Origin of blue straggler stars in the Milky Way halo

Adam Brček

Division of Astrophysics
Department of Physics
Lund University

2023-EXA208

Degree project of 60 higher education credits (for a degree of Master)

Supervisor: Diane Feuillet & Ross Church

Division of Astrophysics
Department of Physics
Box 43
SE-221 00 Lund
Sweden

Origin of Blue Straggler Stars in the Milky Way Halo

Adam Brček

LUND
UNIVERSITY

Master Thesis
Advisors: Dr. Diane Feuillet & Dr. Ross Church
Examiner: Dr. Thomas Bensby

Abstract

Blue straggler stars (BSSs) are exotic stellar objects that appear to be younger than the age of the population they come from suggests. They are observed as the extension of the main sequence stars, beyond the turn-off point. They are present in all types of stellar populations, such as open clusters, globular clusters, dwarf galaxies, and even in the open field. It is believed that they form mainly through binary star evolution. In this work, we are particularly interested in BSSs in the field of the Galactic halo as this is where the ancient dwarf galaxies, that were accreted by the Milky Way, deposited their debris. Studying the BSSs in this part of the Milky Way allows us to not only test the theories of binary star evolution, but it also gives us an insight into some of the oldest stellar populations, which probe the early history of our galaxy. We investigate how these BSSs form, how the theoretical formation channels vary between the accreted (formed ex-situ) and non-accreted (formed in-situ) samples, what the chemical abundance patterns are in the samples, and what that tells us about the populations they come from.

Large datasets are needed to identify these rare stars and we use data from the spectroscopic surveys APOGEE and GALAH, cross-matched with Gaia. The datasets provide the necessary kinematic and chemical information about stars, which allows us to distinguish between stars that formed in the Milky Way and those that formed outside our galaxy, but were eventually accreted into the halo. Since BSSs are thought to form primarily through mass transfer in binary systems, we use the Binary Star Evolution code (BSE) to model possible formation channels for stars in the final sample.

After applying our selection criteria, we end up with a small sample of possible BSSs, and study their chemical abundances and radial velocities. We use some chemical abundances (e.g. barium) to constrain the possible formation scenarios. We generate a large sample of model BSSs using BSE, look at their formation channels, and make synthetic radial velocity measurements, which we compare with the observed values. Lastly, we create detailed theoretical models of formation for two stars in the final sample, which have the radial velocity curve measured.

We find that the vast majority of the stars in the final sample show radial velocity variations, which is consistent with our expectation that they form through binary star evolution. We show that the formation channel of a BSS correlates with its currently observed orbital period and mass. The modeling results show that mainly mass-transfer types B (mass transfer from a red giant), C (mass transfer from an asymptotic giant branch star), and D (accretion of mass from stellar winds) are able to reproduce the observed stars. We conclude that the accreted and non-accreted samples are not inconsistent with being the same. We are largely limited by the small size of the accreted sample of stars. The models also predict higher variation in radial velocity than is observed. Eccentric orbits of BSSs might be able to explain this offset, but our current understanding of binary star evolution cannot easily explain the higher eccentricity in post-mass-transfer systems. This proves to be the case even when modeling the two individual systems, which we are able to recreate accurately through type B or C mass transfer, except for the observed eccentricity.

Popular Summary

We study our galaxy, the Milky Way, through observations of stars in the night sky. They tell us about the structure, composition, and kinematics of different components of our galaxy. Some stars form binaries, which are systems consisting of two gravitationally bound stars that orbit each other. They are great laboratories for testing the current theories of stellar evolution.

Stars of different masses evolve at different rates, which can lead to some interesting interactions. The more massive a star is, the quicker it burns all of its fuel and the shorter it lives. In close binary systems, as the more massive star evolves and expands, its outer layers will not be gravitationally bound to it anymore and they get transferred onto the companion star. As a result, the companion significantly grows in size and becomes a star that we observe as a blue straggler. They are blue because they are massive and hot, and hotter stars emit more energetic blue light. On the other hand, cooler stars appear redder. Blue and hot stars must have formed recently since they live "only" for millions of years, which is quite short on cosmic timescales. However, these young-looking stars have been observed in some of the oldest stellar populations, which are billions of years old. Their presence in these populations is therefore quite puzzling.

The Milky Way is a spiral galaxy consisting of a disk surrounded by a so-called Galactic halo. In this project, we are particularly interested in the halo as it contains some of the oldest stellar populations. During the early history of the Milky Way, there were a lot of interactions with other galaxies. Some dwarf galaxies were gravitationally pulled towards the Milky Way, ripped apart, dissolved, and mixed with other stars. The stars coming from some of these ancient dwarf galaxies are hard to find since they are spread across a large area of the night sky. Luckily, we can find them by studying their motion and chemical composition. Finding blue stragglers in the halo is even more challenging, but they can give us an insight into what these ancient dwarf galaxies looked like.

In this project, we use data from spectroscopic surveys. These are designed to gather and analyze spectra for as many stars as possible, making them great for our science goals as we are looking for very rare objects. These datasets consist of millions of stars, so we need to make reasonable cuts to narrow down the selection. Spectroscopic surveys provide information about the chemical composition of stars, which is useful for our analysis. Stars synthesize different elements during different evolutionary stages and it helps us to better constrain the possible formation mechanisms. When a star transfers its mass onto the blue straggler, it leaves an imprint in its chemical composition, which we can observe in the spectrum.

We study the chemical abundances of blue stragglers that made it into our final sample. We find that the vast majority of these stars are in binary systems, confirming our expectation that they form mainly via mass transfer in binaries. We use computer simulations to model binary systems and investigate how some of the blue straggler stars could have formed. We compare the stars coming from accreted (stars formed outside the Milky Way) and non-accreted (stars formed in the Milky Way) populations, and we do not see major differences in the formation mechanisms of blue stragglers.

Contents

Acknowledgements

Most importantly, I am extremely grateful to my supervisors Dr. Diane Feuillet and Dr. Ross Church for their guidance, encouragement, and all the valuable skills they taught me throughout this project. I would like to thank Dr. Thomas Bensby and Dr. Jens Hoeijmakers for their helpful comments that further improved this thesis. I would also like to thank Dr. Heitor Ernandes for a very insightful discussion about chemical abundances. I would like to give a special thank you to my parents for always supporting me and making my dream of studying astrophysics possible. My deepest gratitude also goes to my fiancé Dylan for always supporting me throughout this journey. Last but not least, I would like to thank my wonderful office mates and the fellow master students for all the fun and inspiring discussions.

Introduction

Blue straggler stars (BSSs) were first identified by Sandage (1953) as the extension of the main sequence (MS) in the color-magnitude diagram (CMD) using photometric observations of the globular cluster M3. They have been extensively studied in stellar clusters, where they are easier to identify since the stars have very similar ages. Stellar clusters have a well-defined turn-off, point in the CMD where the stars start leaving the main sequence as they are running out of hydrogen fuel in their cores. BSSs are less studied in the open field, where they are much harder to identify, since it contains stars of various ages and populations. In this project, we target BSSs in the Galactic halo, which is an old and roughly mono-age population. Coming from old populations, these stars probe the earliest history of our galaxy.

Different formation mechanisms for BSSs have been proposed, and they are most likely the result of binary star interactions. When the more massive star of the binary evolves, it can lose its outer layers as they get accreted by the less massive companion. The companion grows in mass and can end up being more massive than the turn-off mass. Other mechanisms, such as collisions and mergers of stars can also form a BSS. Being a result of binary star evolution, BSSs provide insights into the population they come from, such as the binary fractions. Finding them in the field of the Galactic halo, where accreted satellite galaxies were most likely to deposit their debris, tells us more about these old populations that were dissolved in the Milky Way. Additionally, binary stars are excellent laboratories used to test the theories of stellar structure and evolution. Since we expect them to be the result of mass transfer in a binary system, we can test how well the observed stars correspond to what the theory predicts.

In order to find these rare stars, we need a lot of observations. We use data from the spectroscopic surveys APOGEE and GALAH, which provide radial velocities and detailed chemical abundances for over 1.3 million stars. Knowledge about chemical abundances allows us to distinguish between stars that formed in the Milky Way (in-situ) and those that formed outside the galaxy (ex-situ), but were accreted during a merger event. In addition, certain elements give us clues about the formation history of a star. For example, the lithium and barium abundances are good indicators of whether a system has evolved through mass transfer. Looking at BSSs in the Galactic halo and their formation histories gives us information not only about the Milky Way, but also about the accreted ancient dwarf galaxies.

In this work, we find BSSs in the field of the Galactic halo using photometric and spectroscopic data. After making cuts in the kinematic and chemical space, removing the cluster members, and inspecting the stellar spectra, we end up with a small sample of BSSs, which we study in greater detail. Besides studying the

observed characteristics of the sample (chemical abundances and radial velocities), we also use the Binary Star Evolution code (Hurley et al., 2000, 2002) as the main tool for our analysis. We generate a large number of binaries and make comparisons between the observations and the models. We also make detailed formation models for stars that were previously studied. We are addressing the questions of what the differences are between the accreted and non-accreted samples, how blue stragglers form in the Galactic halo and what that tells us about the environment they are coming from, how we can use the chemical abundances and previous observations to constrain the formation models, and what the differences are between the models and observations.

Chapter 1

Background and theory

1.1 The Milky Way

Large-scale astrometric and spectroscopic surveys allow us to map and study large numbers of stars in unprecedented detail. Our current understanding is that the Solar System is located approximately 8 kpc (GRAVITY Collaboration et al., 2019) from the center of our galaxy, the Milky Way. It consists of several main components: the thin disk, the thick disk, the galactic bulge, and the stellar halo. These components are embedded in a much larger dark matter halo (Figure 1.1).

The thin disk consists of generally younger populations of stars, which follow nearly circular orbits around the Galactic center with low velocity dispersion. The metallicity of stars in the thin disk has a range of $-0.7 < [\mathrm{Fe/H}] < 0.1$ dex, and the $[\alpha/\mathrm{Fe}]$ abundance is nearly solar (Bensby et al., 2014). For chemical abundances, we use the bracket notation defined as

$$[\alpha/\mathrm{Fe}] = \log_{10}\left(\frac{N_\alpha}{N_{\mathrm{Fe}}}\right)_{\mathrm{star}} - \log_{10}\left(\frac{N_\alpha}{N_{\mathrm{Fe}}}\right)_{\odot}, \tag{1.1}$$

where N_X denotes the number of atoms per unit of volume for element X. The thick disk contains older stars, which were kinematically heated through past galaxy mergers, but also via interactions with the spiral arms and giant molecular clouds. Chemically, there is a difference between the thick and thin disk stars. Thick disk stars have lower metallicity and have higher $[\alpha/\mathrm{Fe}]$ abundance (Bensby et al., 2014).

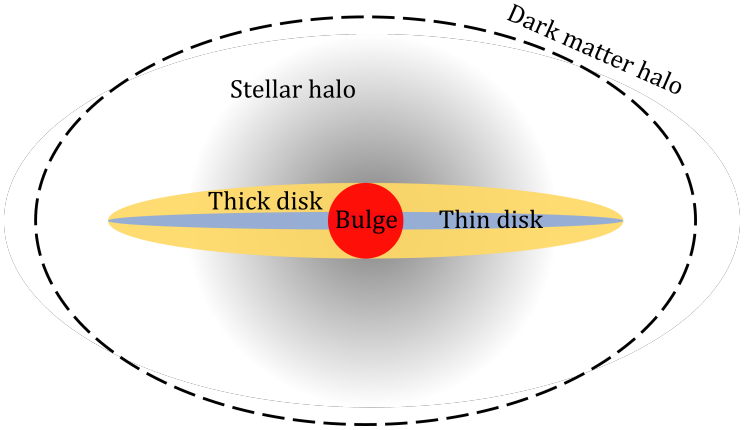

Figure 1.1: Sketch of the main components of the Milky Way.

The Galactic bulge consists mostly of older stars with a large range of metallicity, and it is likely a conglomerate of different stellar populations (Bensby et al., 2017). Studying this part of our galaxy is challenging as it is heavily obscured by dust.

The Galactic halo is thought to have formed early during the galaxy formation process through dissipative collapse and accretion. Orbits of stars in the halo can range from heated disk-like kinematics to retrograde and highly eccentric orbits. Halo stars typically do not have as large of a rotational component to their velocity as disk stars, and they are mostly metal-poor. There has been evidence for two main populations of the halo; one population of former disk or bulge stars that were heated to halo-like kinematics by merging satellite galaxies, and the second population likely having been accreted from ancient dwarf galaxies (Carollo et al., 2007; Nissen & Schuster, 2010).

1.2 Galactic halo and accreted stellar populations

Merger events play a key role in the evolution of a galaxy. These events, that might have happened billions of years ago, can be traced with stars and their chemical and kinematic signatures. The disrupted galaxies that were consumed by the Milky Way were most likely to deposit their debris into the Galactic halo (Helmi, 2020). Looking at these leftover stars does not only tell us more about the formation history of the Milky Way, but also about the ancient galaxies themselves. Dissolved remnants of these galaxies can be observed as stellar streams and stars in the field of the Galactic halo. These stars are estimated to be $10 - 12$ Gyr old (Jofré & Weiss, 2011).

Stars from the same population tend to have similar chemical composition. Chemical tagging is a helpful tool that allows us to determine whether stars come from a common origin based on their chemical signatures, since different elements are formed via different processes. The α-elements, which are formed through the capture of α-particles, have an atomic mass number that is a multiple of 4, i.e. ^{16}O, ^{24}Mg, ^{28}Si, ^{32}S, and ^{40}Ca. These elements are formed in the cores of stars and get expelled into the interstellar medium through type II supernovae (SNe II), while a smaller yield of α-elements is expected to form via type Ia supernovae (SNe Ia). On the other hand, the Fe-peak elements, such as Mn and Ni, are thought to form primarily through SNe Ia (e.g. Arnett, 1996). Hawkins et al. (2015) found that [Mg/Mn]$-$[Al/Fe] chemical space provides a way to chemically distinguish between the accreted and non-accreted stars. Al is important to consider because it forms via SNe II and is sensitive to the initial C and N abundances. Stars coming from accreted populations were found to be underabundant in [Al/Fe]; similar trend holds for [Na/Fe] (Buder et al., 2022). The physical reason for this is still unknown. An example of where the accreted and non-accreted stars lie in these chemical spaces is shown in Figure 1.2 from studies by Das et al. (2020) and Buder et al. (2022).

After the Gaia Data Release 2 (Gaia Collaboration et al., 2018a), several kinematic structures were identified, the largest of which are the Gaia-Sausage (Belokurov et al., 2018) and Gaia-Enceladus (Helmi et al., 2018). It is still unclear whether these two populations correspond to the same accretion event, but it is often referred to as the Gaia-Sausage-Enceladus (GSE). Helmi et al. (2018) found that [Fe/H] of the population is extended at least over 1 dex and has lower [α/Fe] abundance than the thick disk population. This suggests that these stars formed in a system with a different star formation history than the Milky Way and that the

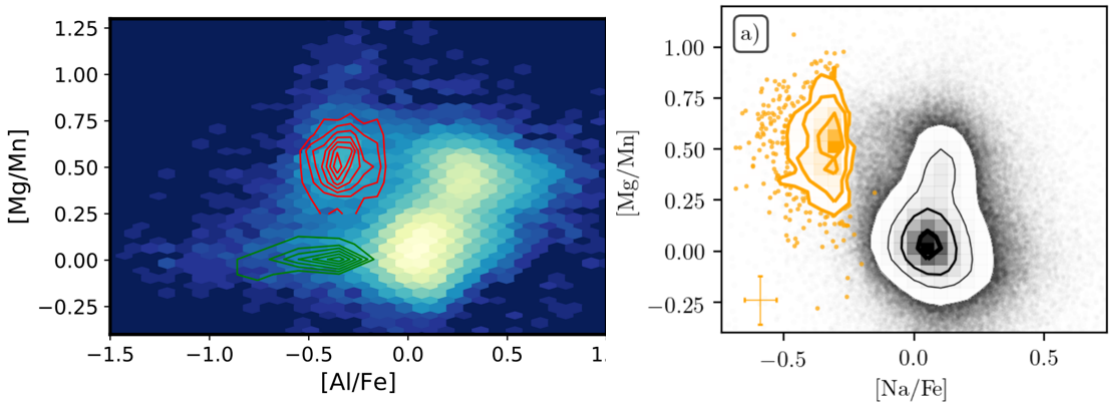

Figure 1.2: Left plot shows the two dimensional abundance distribution in the plane of [Mg/Mn] and [Al/Fe] from Das et al. (2020) using APOGEE DR14. The red contours represent the likely accreted stars, while the green contours are likely low [Al/Fe] thin disk stars. The right plot shows the chemical plane of [Mg/Mn] and [Na/Fe] from Buder et al. (2022) using GALAH DR3. Yellow contours show the chemically selected accreted sample.

stars were accreted. After the initial star formation, the most massive stars explode as type II supernovae and enrich the environment in a way that [α/Fe] abundance remains roughly constant. Type Ia supernovae, which produce primarily Fe-peak elements, require the formation of white dwarfs, so there is a delay between the enrichment from type Ia and type II supernovae (e.g. Nissen & Schuster, 2010). GSE is an old population with estimated age of $10 - 12$ Gyr and mean metallicity [Fe/H] ≈ -1.15 dex (Feuillet et al., 2020, 2021). The deficiency in α-elements is present in some satellite galaxies as well. From chemical abundance analysis of the Sagittarius dwarf galaxy, McWilliam et al. (2013) conclude that α-element deficiency is not caused by the SN Ia time-delay scenario (i.e. slower star formation rate compared to the MW), but is instead caused by an initial mass function deficient in the highest mass stars. Abundance similarities with the Large Magellanic Cloud, Fornax, and IC1613 suggest that this is the case even for these dwarf galaxies.

1.3 Binary stars

In order to understand how blue straggler stars form in stellar populations, we need to consider binary star evolution. A binary star is a system of two stars that are gravitationally bound to each other. In the case of very wide-orbit binaries, each star evolves separately and the binary system remains stable for most of its lifetime. However, if they are close enough, they can interact, exchange mass or fully merge. For example, in a binary system consisting of two MS stars of different masses, the more massive one evolves into a red giant faster. Its envelope expands, the outer layers of the star are not gravitationally bound to it anymore, and they get accreted by the companion star. Binary stars are excellent tools to study and test the stellar structure and evolution theory. They can be used to determine the masses and luminosities for stars independent of their distance. They also serve as laboratories for the study of mass transfer between stars and its effect on stellar evolution, and by the study of their orbital dynamics, we can probe the deep internal density structures of the constituent stars (Meyers, 1992).

Binary stars can be observed in a number of ways. In visual binary systems, both components are resolved and visible. Astrometric binaries provide indirect evidence for the presence of an unseen companion star through the motion of the visible star. Binaries can also be observed through the periodic Doppler shift of their spectral lines. If spectral lines of both stars are visible, it is a double-lined spectroscopic binary (SB2) and if only one set of lines is visible, it is a single-lined spectroscopic binary (SB1). In a special case, when the plane of orbit of the two stars is seen edge on, periodic eclipses can be observed using photometry, and we refer to this system as an eclipsing binary.

1.3.1 Binary interactions

The main tool used to describe the orbits of binary stars are the three Kepler's laws for planetary motion in their generalized form. Firstly, the orbits are conic sections and bound orbits are ellipses. Secondly, the line connecting the two bodies sweeps out equal areas in equal time. Lastly, the period P and semi-major axis a are related by

$$\left(\frac{P}{2\pi}\right)^2 = \frac{a^3}{G(M_1 + M_2)}, \tag{1.2}$$

where G is the gravitational constant, and M_1 and M_2 are the masses of the two stars (Eldridge & Tout, 2019).

The region around the star in which material is gravitationally bound to the star is called its Roche lobe. It is a bounding equipotential surface in the frame of reference, in which the stars are stationary. In a binary system, each star has its Roche lobe, the radius of which can be approximated as (Eggleton, 1983)

$$r_L = \frac{0.49q^{2/3}}{0.6q^{2/3} + \ln\left(1 + q^{1/3}\right)}, \tag{1.3}$$

where q is the mass ratio of stars and r_L is then given in the units of the orbital separation. As the more massive star in the binary system evolves and expands, it can fill its Roche lobe. This results in mass transfer between the stars as the outer layers of the more massive star are not gravitationally bound to it anymore and get transferred onto the companion star. This is called Roche lobe overflow.

There are four main types of mass transfer depending on which evolutionary stage the primary star is at when it starts filling its Roche lobe. Type A mass transfer refers to the case when the star that is filling its Roche lobe is a main sequence (MS) star. This type of mass transfer generally results in a contact system and eventually in a merger (Paczyński, 1971). Type B mass transfer occurs when the star filling its Roche lobe is on the red giant branch (RGB). Initial orbital periods of these binaries can range from a few days to hundreds of days (Paczyński, 1971). After stable mass transfer, the system can be observed as a single-lined spectroscopic binary, where the secondary star is a helium white dwarf. Type C mass transfer occurs when the Roche lobe filling star is on the asymptotic giant branch (AGB). Initial orbital periods of these systems can range from hundreds to thousands of days (Paczyński, 1971). The post-mass-transfer system contains a carbon-oxygen white dwarf. There is also a type D mass transfer, which refers to the case when an AGB star has strong stellar winds and some of that material gets accreted by the companion. This can happen in binaries with long orbital periods ($P > 1000$ days), but it is not an effective way of mass transfer (Abate et al., 2013).

1.3.2 Blue straggler stars

Sandage (1953) first observed blue straggler stars (BSSs) as the apparent extension of the classical main sequence in the color-magnitude diagram (CMD). These stars are more massive than the turn-off mass and therefore should have already evolved off the stellar main sequence. They appear to be younger than the age of the populations they come from. With our current understanding, they cannot be explained via evolution of a single star, but they can form through direct stellar collisions and binary star evolution (Knigge et al., 2009). BSSs are present in all types of stellar populations: globular clusters, open clusters, but even in the open field and ultra-faint dwarf galaxies. BSSs can be observed in some systems better than others as they only stand out in the CMD for a population of stars of the same age. They are hard to spot in e.g. the thin disk, which consists of stars with a wide range of ages. In very low-density systems, mass transfer and mergers of binaries or multiple systems are the main formation mechanisms for blue stragglers (Santana et al., 2013). Binary processes seem to be the main formation channel even in higher density environments. As the stellar density increases, the specific frequency of blue stragglers starts to decrease at sufficiently high densities. This is unexpected if BSSs are formed through stellar collisions. It might suggest that with increasing stellar density, the collision rate increases, but binaries that would have formed BSSs get disturbed (Sills, 2016).

As a consequence of the anticorrelation of close binary fraction with metallicity (Moe et al., 2019), the fraction of BSSs also increases when looking at increasingly metal-poor populations (Wyse et al., 2020). This can be explained by the fragmentation model of molecular cores. With decreasing metallicity, the expected infall rates from hotter cores increase, and the temperatures of the optically thick disks decrease. Both of these mechanisms drive the disk towards instability and fragmentation. In case of the Sagittarius dwarf galaxy, after comparing stars with similar stellar parameters, it has been found that the fraction of close binaries is intrinsically higher than in the Milky Way (Bonidie et al., 2022). This provides evidence that environments of ellipticals, spirals, and dwarf galaxies should lead to different field binary fractions for MS stars. The physical reason for this is not yet understood.

Some chemical abundances in BSSs provide clues about the formation history of these systems. Barium abundance in BSSs can be an indicator that they formed via mass transfer from an AGB star. Slow neutron capture (*s*-process) elements, like barium, are synthesized during thermally pulsing AGB phase of stellar evolution (e.g. Gallino et al., 1998). During mass transfer, the AGB donor pollutes the surface of the BSS and enhances its [Ba/Fe] abundance. These so-called barium stars have been extensively studied as G and K-type giants (Bidelman & Keenan, 1951) or F, G, and K-type main-sequence stars (North et al., 2000) enriched in *s*-process elements. Milliman et al. (2015) studied the surface barium abundance of BSSs in NGC 6819 and found 5 BSSs significantly enriched in barium with [Ba/Fe] between +0.48 and +1.36 dex. They conclude that mass transfer from an AGB companion is indeed able to produce this amount of barium enrichment. North et al. (2000) show that the vast majority of observed barium dwarfs were in a binary system. These barium dwarfs, along with barium giants in binary systems, have orbital periods between 100 and 10^4 days, with most of the short-period (< 1000 days) systems in circular orbits. Some of the observed systems also have high eccentricity, which is not easy to explain for a post-mass-transfer system, the orbit of which should be

circularized. Reduced circularization efficiency can explain some of these systems (Escorza et al., 2020).

Another element of interest is lithium, which is fragile in stellar interiors and gets destroyed at temperatures of $\approx 2.5 \times 10^6$ K (Pinsonneault, 1997). Lithium abundance drops for cooler stars with deeper convective envelopes as the lithium gets transferred into the hotter interior of the star, where it gets destroyed. It is also expected to be depleted during the process of mass transfer due to the mixing (Carney et al., 2001). Lithium in metal-poor halo dwarf stars has been shown to be independent of temperature and metallicity, forming the so-called "Spite plateau" (Spite & Spite, 1982) at A(Li) ≈ 2.2, where A(Li) is defined as

$$\mathrm{A(Li)} = \log_{10}\left(\frac{N_{\mathrm{Li}}}{N_{\mathrm{H}}}\right) + 12. \tag{1.4}$$

For the conversion from [Li/Fe] to A(Li), we use the value $\log_{10}(N_{\mathrm{Li}}/N_{\mathrm{H}})_{\odot} = -11.04$ (Asplund et al., 2021). Another feature observed in the lithium abundance is the "lithium dip", which refers to the significant drop in the Li abundance for main sequence stars with effective temperatures between 6400 and 6850 K (Gao et al., 2020). The location of the gap in the $T_{\mathrm{eff}} - \log\ g$ space (Kiel diagram) is shown in Figure 1.3. Higher lithium abundances are observed on both cooler and hotter side of the lithium dip. Stars on the hotter side have the shallowest convective zones and internal mixing is not as prominent. As the temperature drops, the convective zones become deeper and are able to effectively destroy the lithium, which is observed as the lithium dip. On the cooler side of the dip, convective envelopes are even deeper, but the higher observed lithium abundances can be explained by internal gravity waves. These efficiently extract angular momentum from the interior and this process counter-acts the rotational mixing (Charbonnel & Talon, 2005).

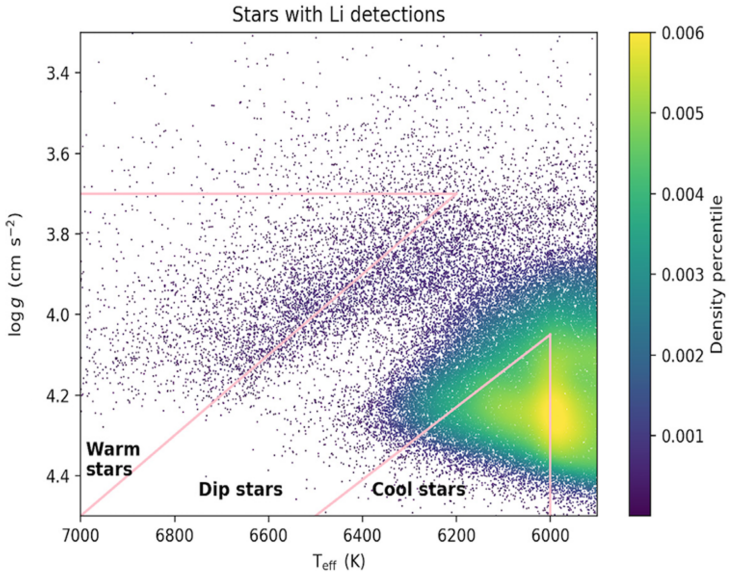

Figure 1.3: Kiel diagram of mainly dwarf and sub-giant stars with [Fe/H] ranging from -3.0 to 0.5 dex from Gao et al. (2020). Only stars with lithium detection are plotted. The lithium gap is prominent in the diagonal region between $T_{\mathrm{eff}} \approx 6300$ to 6600 K, with surface gravity $\log g$ ranging from 3.8 to 4.3 dex.

Other abundance signatures of mass transfer include carbon and oxygen depletion, which could hint towards a BSS formed via case B mass transfer, when the accreted material eventually comes from deep within the star, where partial CNO processing has occurred. It is possible that this depletion is observed only in recently born BSSs, which are expected to rotate more rapidly. As the star evolves and the rotation slows down, mixing might be introduced which would bring the C and O abundances close to normal values (Ferraro et al., 2006). Lastly, high-mass stars with low N/C surface density ratios could be the products of mergers and mass transfer during or after the first dredge up phase, when the CN cycled material is brought to the surface (Hekker & Johnson, 2019).

In this work, we use data from the spectroscopic surveys APOGEE and GALAH, in which we try to target BSSs in the field of the Galactic halo. Using chemical abundances, we can divide the stars into accreted and non-accreted samples. Are there any major differences between the two samples? Can we determine how some of these stars formed? Do some stars have special abundance pattern (e.g. enrichment in *s*-process elements), suggesting that they formed via mass transfer in a binary system? What does the overall population of BSSs in the Galactic halo tell us about the formation history of the Milky Way and ancient dwarf galaxies? To answer some of these questions, we gather more information about the chemical abundances and radial velocities of the BSSs from previous literature and the spectroscopic surveys. We use the Binary Star Evolution code to create a synthetic population of blue stragglers, for which we make synthetic radial velocity measurements. We compare the generated sample with the observed stars, look at the formation channels for the BSSs, and for some systems, we can make a detailed model of their formation constrained by the observables.

Chapter 2

Data and selection

2.1 APOGEE

The Apache Point Observatory Galactic Evolution Experiment (APOGEE) is a large-scale, stellar spectroscopic survey, and one of the programs in the Sloan Digital Sky Survey (SDSS). It is based on the observations from the 2.5-meter Sloan Foundation Telescope and the 1-meter New Mexico State University Telescope in New Mexico. The survey also covers the southern hemisphere using the 2.5-meter Irénée du Pont Telescope of Las Campanas Observatory in Atacama de Chile. The survey was designed to address the problem of galaxy formation through the chemical and kinematic study. It is conducted in the near-infrared (H-band, $1.5-1.7$ μm), allowing the study of stars hidden behind dust. The spectrographs on the telescopes provide high-resolution spectra ($R \approx 22500$) predominantly for RGB stars and other luminous post-main-sequence stars (Majewski et al., 2017). In this work, we use the Data Release 17 (Abdurro'uf et al., 2022), which is the final data release for the APOGEE survey.

APOGEE has a complex selection function, and blue and hot stars are not the main focus of the survey. The selection for the main program has a color cut $(J - K_s)_0 \geq 0.5$, where J and K_s are 2MASS magnitudes. This corresponds to $(\mathrm{BP}-\mathrm{RP})_0 \geq 1$ (calculated using conversion from Gaia Collaboration et al. (2018b)), which is much redder than we would observe in BSSs, and the cut automatically removes the stars we are interested in. For all halo programs, the color cut is $(J-K)_0 \geq 0.3$, corresponding to $(\mathrm{BP\text{-}RP})_0 \geq 0.7$, which places the color cut roughly at the turn-off of the halo population. However, hotter stars than the selection cut are often selected for telluric calibration since they lack strong spectral features or they could have been selected as a part of other survey programs. Taking the selection function into account would be a complicated task, and we do not attempt to correct for selection biases.

Determining precise chemical abundances in hotter stars ($T_{\mathrm{eff}} > 6000$ K) can be challenging as atomic lines get weaker. This is important to consider, since the majority of stars in our final sample have $T_{\mathrm{eff}} > 6000$ K. When it comes to the reliability of determined abundances in dwarf stars, the APOGEE team lists C, Mg, Si, Fe, Ni as the most reliable, C I, O, Al, K, Ca, Mn as reliable, N, S as less reliable, P, Ti II, Co, Cu, Ce, Nd as unsuccessful, and Ge, Rb, Yb as not attempted. APOGEE's target for precision in chemical abundances is a signal-to-noise ratio of 100 per pixel, but most elements can be well measured down to signal-to-noise ratio

of 70. Each star in the dataset also has flags listed, which inform the user if there were any issues with the data reduction. We inspect the `ASPCAPFLAG` and `STARFLAG` for any indications of bad data.

2.2 GALAH

The Galactic Archaeology with Hermes (GALAH) survey is another stellar spectroscopic survey, providing detailed chemical abundances for a large number of stars in the southern sky. The survey uses the 4-meter Anglo-Australian Telescope at the Siding Spring Observatory in Australia. The HERMES spectrograph is capable of measuring high resolution spectra ($R \approx 28000$) in four bands, mostly in the optical part of the spectrum: blue ($4716 - 4896$ Å), green ($5650 - 5868$ Å), red ($6480 - 6734$ Å), and near-infrared ($7694 - 7876$ Å) (Buder et al., 2018). In this work, we use the Data Release 3 (Buder et al., 2021).

There is not a strict color cut, so we would expect to see more stars in the blue straggler region of the CMD. Similarly to the APOGEE data, we need to be careful when using the determined abundances. For hot stars above 6000 K, a systematic trend causing increasingly underestimated effective temperature was identified. The absolute accuracy value for the effective temperature is likely underestimating the uncertainty for the hottest stars (Buder et al., 2021).

2.3 Gaia, extinction, distances, and orbits

The data from the spectroscopic surveys are cross-matched with Gaia Data Release 3 (Gaia Collaboration et al., 2022). Gaia is an all-sky astrometric and photometric survey, the goal of which is to chart a three-dimensional map of the Milky Way. In the latest data release, Gaia offers astrometric solutions for almost 1.5 billion stars and radial velocity measurements for approximately 33 million stars. Proper motions and parallaxes from Gaia are necessary to determine the orbit of stars.

In order to calculate the orbits, we use the right ascension, declination, and proper motions from Gaia DR3. We use the radial velocity determined from APOGEE or GALAH, and photo-geometric distances from Bailer-Jones et al. (2021). Orbits are calculated with `galpy` (Bovy, 2015) using the `MWPotential2014` (Bovy & Rix, 2013). Finally, we use the `StarHorse` catalog (Queiroz et al., 2020) to obtain the dereddened color and extinction in the G-band, in order to create an accurate CMD. The absolute magnitude corrected for extinction is calculated as

$$M_G = G - 5\log_{10} d + 5 - A_G, \tag{2.1}$$

where G is the G-band photometric magnitude, d is the distance to the star in pc, and A_G is the extinction in the G-band.

2.4 Selection

The selection criteria are summarized in Table 2.1. We make an initial parallax cut and select only stars that have a relative uncertainty in parallax σ_p/p less than 20%. This helps to exclude stars with very uncertain distance measurements. After calculating the orbits, we select stars with tangential velocity in galactocentric

Table 2.1: Selection criteria for halo stars.

Quantity	Value
σ_p/p	< 0.2
V_T	< 100 km/s
[Fe/H]	< -0.5 dex
S/N (APOGEE)	> 80
S/N (GALAH)	> 30

coordinates below 100 km/s. In Figure 2.1, which shows the tangential velocity V_T versus the radial velocity V_R, disk stars form the overdensity at $V_R \approx 0$ and $V_T \approx 220$ km/s. These are stars on mostly circular orbits with little radial motion. We expect to find the halo stars below the 100 km/s line. These stars have radially extended, eccentric orbits, and a lot of them are even in retrograde orbits. The Galactic halo consists of metal-poor populations, e.g. the metallicity distribution function for Gaia-Sausage-Enceladus suggests that vast majority of stars have [Fe/H] below -0.5 dex (Feuillet et al., 2021). We therefore limit the metallicity [Fe/H] to be less than -0.5 dex, which further helps to remove any disk stars. We then make a quality cut on the spectra and select only those with signal-to-noise ratio greater than 80 for APOGEE stars, and greater than 30 for GALAH stars.

As the next step, we make a selection in the CMD. The region selected is shown in Figure 2.2. Blue stragglers can be found as the extension of the main sequence, so we try to target that region of the CMD. We make a rather generous selection, selecting stars just below the horizontal branch and also above the sub-giant branch as this region might contain evolved blue stragglers.

We use chemical tagging to distinguish between stars coming from accreted populations and those that formed in the Milky Way. Following the method of Das et al. (2020), we use the [Mg/Mn]$-$[Al/Fe] chemical abundance space for the APOGEE stars. Motivated by the results shown in Figure 1.2, we define a boundary between the accreted and not accreted stars at [Al/Fe] $= -0.15$ (Figure 2.3). We refer to

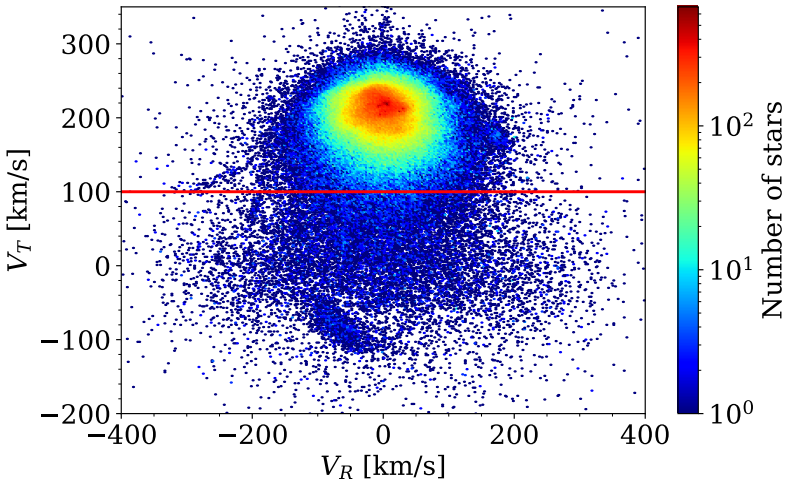

Figure 2.1: Tangential velocity versus the radial velocity in galactocentric coordinates for the APOGEE sample. Disk stars form the overdensity at $V_R = 0$ km/s. We select the stars below the red horizontal line, where we expect to find halo stars.

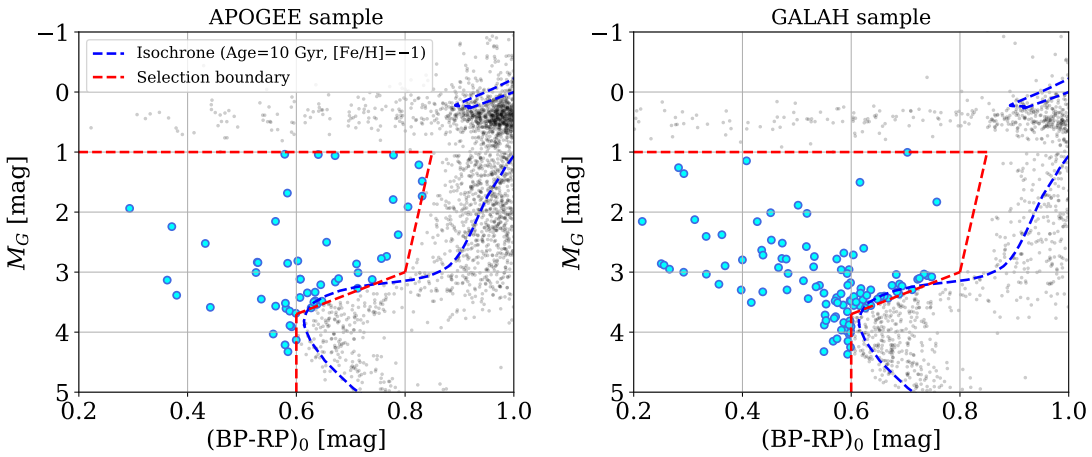

Figure 2.2: Color-magnitude diagram selection for the APOGEE sample (left) and the GALAH sample (right). Boundary for selection is shown as the red line, defined by points [0.6, 5], [0.6, 3.7], [0.8, 3], [0.85, 1], [0.2, 1]. Black points in the background show stars in the halo selection (stars after applying the criteria in Table 2.1) from APOGEE (left) and GALAH (right). A `PARSEC` isochrone (Bressan et al., 2012) of a halo-like population is shown as the blue line.

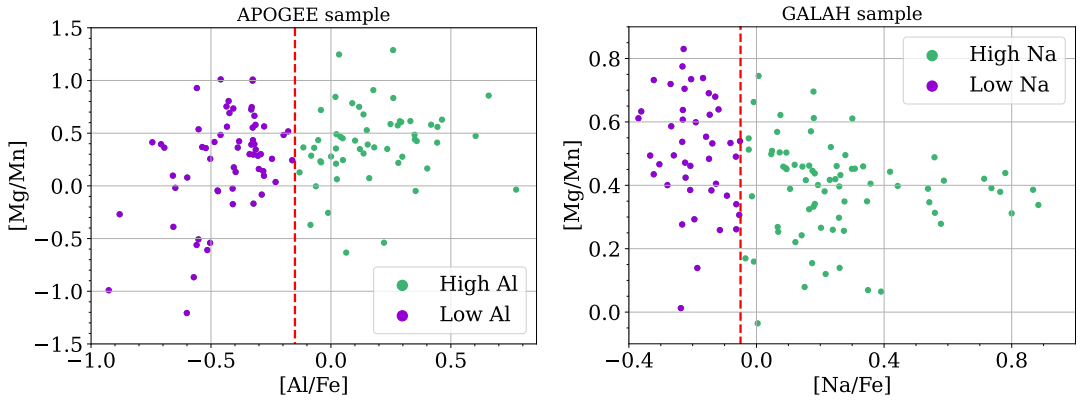

Figure 2.3: Selecting accreted and non-accreted stars using the [Al/Fe] abundance in the APOGEE sample (left) and [Na/Fe] abundance in the GALAH sample (right). High Al and high Na stars correspond to stars formed in-situ, while the low Al and low Na stars are of possible accreted origin.

stars below this threshold as "low Al" or "accreted" population, while stars above this value are "high Al" or "non-accreted" stars. This is consistent with findings of Das et al. (2020), and making the cut only in [Al/Fe] also allows us to include stars that do not have Mg or Mn abundances measured. In case of the GALAH sample, we use the findings of Buder et al. (2021) and replace [Al/Fe] with [Na/Fe], since the GALAH stars do not have reliable Al abundance measurements. We define a boundary at [Na/Fe] $= -0.05$, which separates "low Na" or "accreted" stars from "high Na" or "non-accreted" stars (Figure 2.3).

In order to obtain stars that are in the field of the Galactic halo, we need to remove any cluster members. In case of APOGEE, the survey was conducted along a number of different lines of sight, each referred to as a "field". If a certain field contains a stellar cluster, the field is named after that cluster. We test the membership of a specific star to a cluster by plotting all the stars within one field in the line-

of-sight velocity versus metallicity space, then we plot the stars in the final sample over them. Cluster members tend to create clumps in this space as the stars from one cluster have similar chemical composition and also move at a similar velocity from or towards us. If the stars tested for membership fall onto the clump created in this space, we assume they belong to the cluster, and they are excluded from the selection. The method is demonstrated for the stars in the NGC6397 field in Figure 2.4. In case of GALAH, the fields are not so conveniently named, and we need to take a different approach. We use the Milky Way Star Clusters catalog (Kharchenko et al., 2013) and compare the positions of known clusters with the positions of stars in our sample. If there was a match (star within 0.25° from the location of cluster), line-of-sight velocity and metallicity were considered to determine the membership. All cluster members were excluded.

2.5 Spectra inspection and final sample

Our analysis relies heavily on the [Al/Fe] and [Na/Fe] measurements. We therefore inspect all the spectra individually, focusing on the main Al spectral lines (in case of APOGEE) and the main Na lines (in case of GALAH). If no lines are visible, the star is excluded. To test the reliability of abundance measurements, we use twin stars, i.e. stars with similar stellar parameters (effective temperature, metallicity, surface gravity) to the star we are interested in, but with slightly higher Al or Na abundance. Comparing the two spectra, we should see that the Al or Na lines in the twin spectrum are slightly deeper. This process is shown in Figure 2.5 for one APOGEE star, which made it into the final sample.

Following the procedure for all stars results in the final sample. CMDs for these stars are shown in Figure 2.6. Kiel diagrams (surface gravity vs. effective temperature) are shown in Figure 2.7. We then use the SIMBAD database (Wenger et al., 2000) to gather more information about the stars in the final sample. Additionally, we also check the binary catalogs for APOGEE (Kounkel et al., 2021) and GALAH (Traven et al., 2020). Kounkel et al. (2021) identify double-lined and higher or-

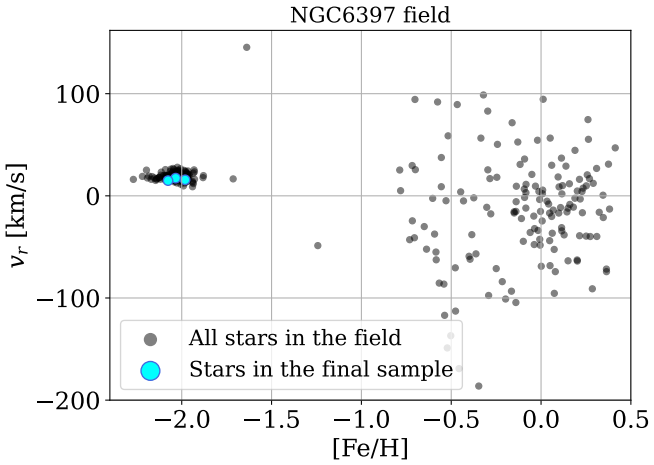

Figure 2.4: Testing cluster membership in the line-of-sight velocity and metallicity plane. All stars in the NGC6397 APOGEE field are plotted and tested stars are plotted over them. In this case, the tested stars fall onto the clump, they belong to the cluster, and were therefore excluded from further analysis.

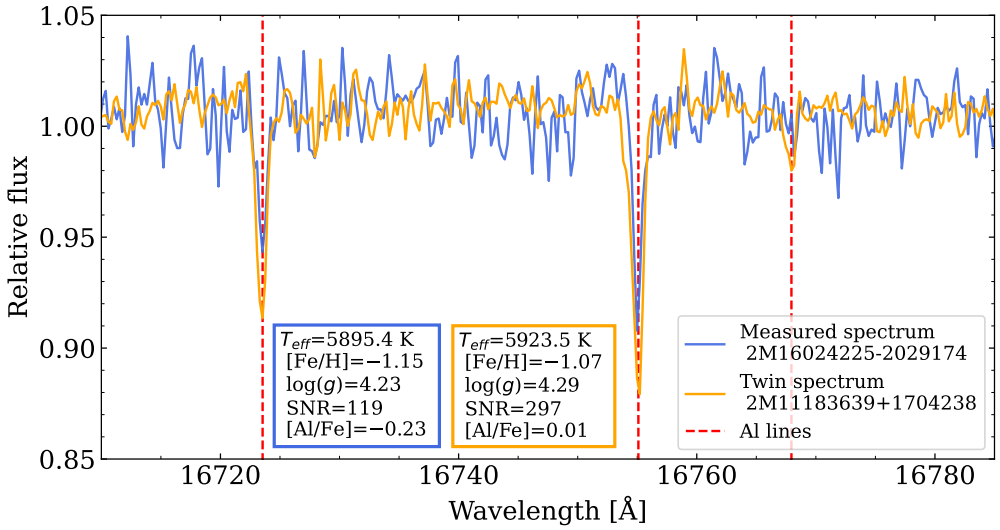

Figure 2.5: Region of the spectrum containing the main Al lines for one APOGEE star that made it into the final sample. Twin spectrum of a star with similar stellar parameters, but higher [Al/Fe] abundance, is plotted over it. The twin spectrum shows slightly deeper Al lines.

der spectroscopic binaries using Gaussian deconvolution of the measured spectra. Traven et al. (2020) take a more complex approach and also include astrometry and photometry in their analysis, but they only look at double-lined spectroscopic binaries. Parameters for all stars in the final selection can be found in tables in Appendix A.

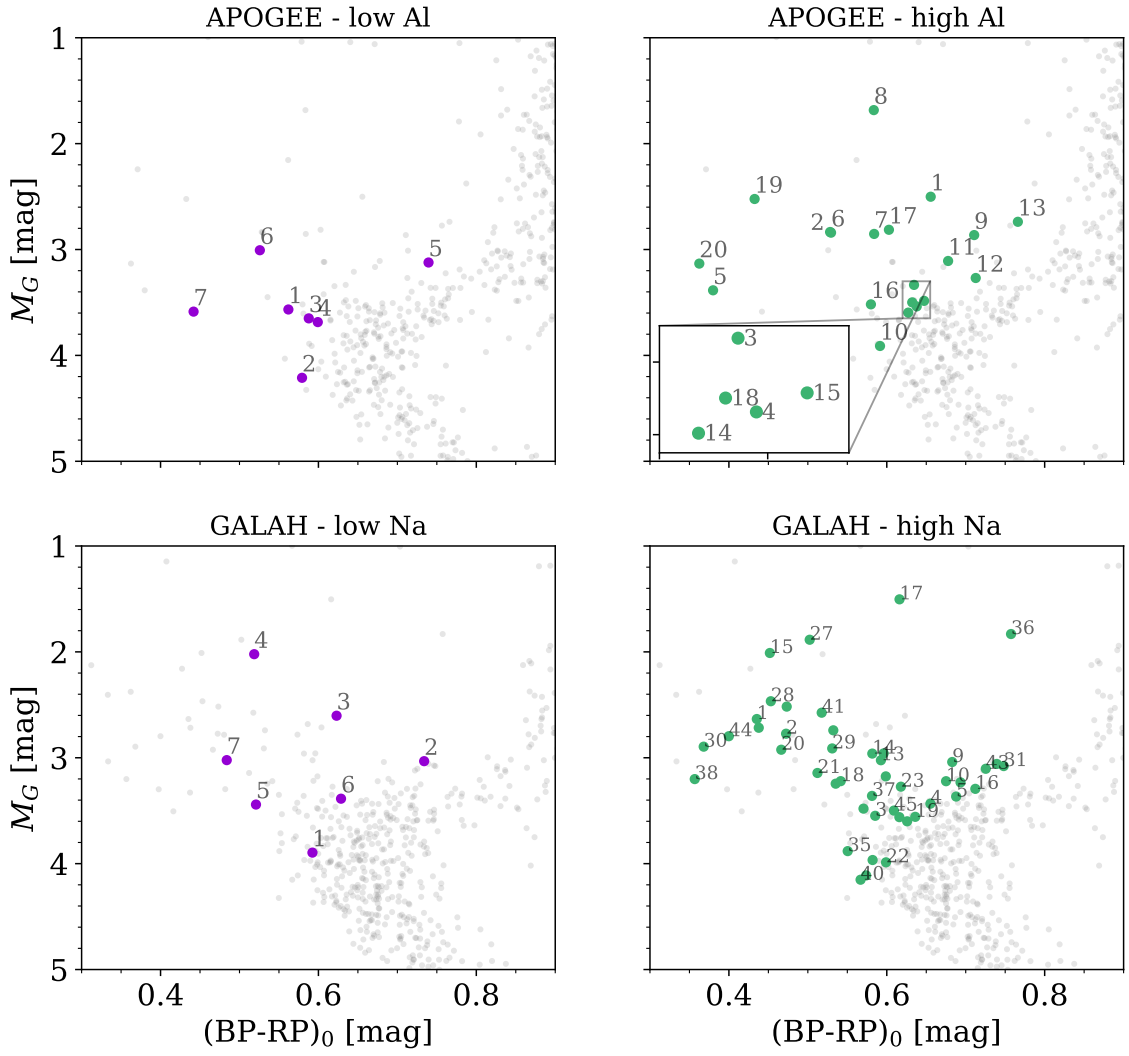

Figure 2.6: CMDs showing the stars in the final sample from APOGEE (top panels) and GALAH (bottom panels). Purple points show stars of possible accreted origin and green points show stars formed in-situ. Background shows the halo stars (stars after cuts shown in Table 2.1). Each star has a number index, see Appendix A for details about each star.

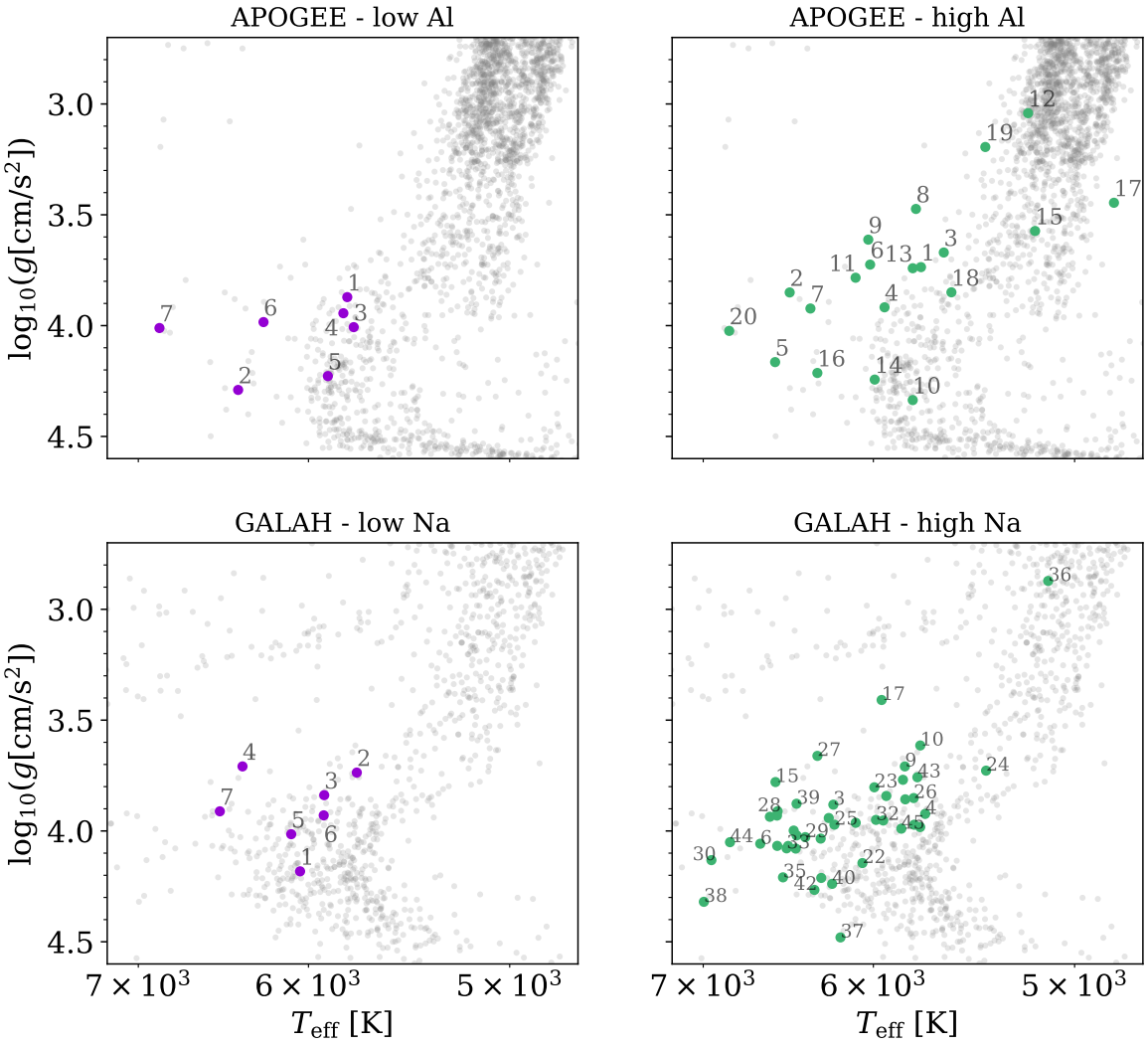

Figure 2.7: Kiel diagrams showing the stars in the final sample from APOGEE (top panels) and GALAH (bottom panels). Purple points show stars of possible accreted origin and green points show stars formed in-situ. Background shows the halo stars (stars after cuts shown in Table 2.1). Each star has a number index, see Appendix A for details about each star.

Chapter 3

Methods

3.1 Binary Star Evolution code

To model the formation of the BSSs in the final sample, we use the Binary Star Evolution code (BSE, Hurley et al., 2002). It is a population synthesis code, which is used to rapidly calculate the evolution of stars and stellar systems. Full structures of the stars are not resolved, but stars are represented by analytical fits and interpolations from detailed stellar evolution codes. The algorithm includes mass transfer, mass accretion, common-envelope evolution, collisions, supernova kicks, tidal interactions, and others.

Since our sample consists of a large variety of stars with different data available, we need to take different approaches with the modeling. For the majority of stars, we have the stellar parameters, chemical abundances, magnitudes, and only a few radial velocity (RV) measurements. We can use these observables to estimate the stellar mass and the amplitude of the radial velocity curve. One approach is to generate a large number of BSSs using BSE, assume that stars in the same region of the CMD behave similarly, and then look at the formation channels that are required to end up in that particular region of the CMD. Additionally, we make synthetic RV measurements of the generated sample, and test how those values compare to the observed ones.

To make a detailed model of formation, we need to know the full shape of the RV curve. This gives us information about the eccentricity and orbital period of the system. Along with the chemical abundances, this allows us to make a detailed model of formation. Through least-squares fitting, we can determine what set of initial parameters ends up in a BSS that corresponds with the currently observed mass and orbital period.

3.1.1 Modifications of the code

Following the method of Vos et al. (2020), we make a few modifications to the BSE code. The critical initial mass ratio for stable mass transfer from a red giant is significantly underestimated in the default implementation. Pavlovskii & Ivanova (2015) found that the critical initial mass ratio varies from 1.5 to 2.2, and in underdeveloped giants, this ratio may be even higher. We therefore change the stability

criterion for this type of mass transfer to

$$q_i = \frac{M_{\rm primary}}{M_{\rm companion}} \leq 2.1\ . \tag{3.1}$$

In addition, the code has been modified to produce mass loss with the angular momentum of the accretor, and the thermal limit on the red giant mass transfer rate has been removed.

We also implement an updated prescription for equilibrium tides from Preece et al. (2022). They show that the default prescription significantly overestimates the strength of tidal dissipation for certain types of stars. We replace the default prescription of $(k/T)_c$ for convective damping, where k is the apsidal motion constant and T is the tidal response time, by the following

$$\left(\frac{k}{T}\right)_c = \left(\frac{R_{\rm conv}}{R}\right)^{a(z)} \left(\frac{M_{\rm conv}}{M}\right)^{b(z)} \frac{c(z)}{t_{\rm conv}}, \tag{3.2}$$

where $R_{\rm conv}$ is the radial thickness of the convective envelope, $M_{\rm conv}$ is its mass, R is the total radius of the star, M is the total mass, $t_{\rm conv}$ is the convective turnover time (we use the default definition), and $a(z)$, $b(z)$, $c(z)$ are coefficients dependent on metallicity, defined as follows

$$a(z) = 0.63 \log_{10} z + 2.72, \tag{3.3}$$

$$b(z) = -0.219 \log_{10} z + 0.68, \tag{3.4}$$

$$c(z) = -0.023 \log_{10} z + 0.22. \tag{3.5}$$

Preece et al. (2022) also provide a prescription for the convective core, but we do not implement this type of convective damping. The transition from radiative to convective core occurs around 1.2 $M_\odot$ (Padmanabhan, 2001) and we are not considering masses larger than that.

3.1.2 Fitting the data

For some stars in our final sample, the RV curve has been measured in previous studies, which allows us to constrain the models. In the case of having n observables $x_{\rm obs}$ with uncertainty $\sigma_{\rm obs}$ and values generated by the model x, we can find the best fit by minimizing the χ^2 function defined as

$$\chi^2 = \sum_{i=1}^{n} \frac{(x_i - x_{{\rm obs},i})^2}{\sigma^2_{{\rm obs},i}}. \tag{3.6}$$

3.1.3 Population synthesis

We make a large population of binaries to analyze the formation channels for a large number of model BSSs. For the mass of the primary, we use the initial mass function (IMF) from Kroupa (2001), which is defined as

$$\xi(m) \propto m^{-\alpha}, \tag{3.7}$$

where $\xi(m)\mathrm{d}m$ is the number of single stars in the mass interval m to $m + \mathrm{d}m$, and α is defined as

$$\alpha = \begin{cases} 1.3, & 0.08\ M_\odot \leq M_* < 0.5\ M_\odot \\ 2.3, & M_* \geq 0.5\ M_\odot. \end{cases} \tag{3.8}$$

The secondary masses are determined from the mass ratio which is drawn from a uniform distribution between 0 and 1 (Moe & Di Stefano, 2017). We use the log-normal distribution for initial orbital period of binaries from Raghavan et al. (2010). We consider a flat eccentricity distribution, since Preece et al. (2022) show that the differences in population synthesis results obtained through different eccentricity distributions are small.

After generating the populations, we make a few more calculations. We calculate the surface gravity of stars as

$$\log g = \log_{10}\left(\frac{GM}{R^2}\right), \tag{3.9}$$

where G is the gravitational constant, M is the mass of the star and R is its radius. BSE uses the metallicity Z as the mass fraction of all elements heavier than helium. We make a conversion to [Fe/H] as

$$[\mathrm{Fe/H}] = \log_{10}\left(\frac{Z}{0.0196}\right), \tag{3.10}$$

Where we use $Z_\odot = 0.0196$ (Vagnozzi, 2019). We then calculate the absolute magnitude in the Gaia bands using bolometric corrections from Casagrande & VandenBerg (2018), which take T_{eff} (up to 8000 K), $\log g$, and [Fe/H] as input. Absolute magnitude in the G-band is then given as

$$M_G = M_{\mathrm{bol},\odot} - 2.5\ \log_{10}\left(\frac{L_{\mathrm{bol}}}{L_\odot}\right) - BC_{\mathrm{G}}, \tag{3.11}$$

where $M_{\mathrm{bol},\odot} = 4.74$ is the bolometric magnitude of the Sun, L_{bol} is the bolometric luminosity obtained from BSE, and BC_G is the bolometric correction for the G-band. The same procedure was applied to the G_{BP} and G_{RP}-bands. In case of both stars having comparable luminosities $M_{G,1}$ and $M_{G,2}$, we need to consider the incoming flux from both stars. We obtain the total G-band magnitude as

$$M_{G,\mathrm{tot}} = -2.5 \log_{10}\left(10^{-0.4M_{G,1}} + 10^{-0.4M_{G,2}}\right). \tag{3.12}$$

3.2 Synthetic radial velocity measurements

The vast majority of stars in our final sample only have a few RV measurements. To make comparisons between the final sample and the generated population, we make synthetic RV measurements of the synthesized population of binaries. In order to do so, we need to obtain the amplitude of the RV curve and the inclination of the binary system. We also need to take into account the orbital period of the system since the RV of a long period binary will not change much in a short time-span of observations. We obtain a synthetic measurement of the radial velocity as

$$v_{r,\mathrm{obs}} = v_K \sin(i) \sin(\theta), \tag{3.13}$$

where v_K is the Keplerian velocity of the BSS in the binary orbit, i the inclination of the system defined as the angle between the line of sight and the vector perpendicular to the plane of orbit of the binary, and θ is the orbital phase.

To derive v_K, we first need to consider the pericenter and apocenter distances, which are given as

$$r_p = a(1-e), \quad r_a = a(1+e), \tag{3.14}$$

where $a = a_1 + a_2$ is the semi-major axis of the orbit and e is the eccentricity. The angular momentum is conserved, so the following must be true for the specific angular momentum

$$j = v_p r_p = v_a r_a = \sqrt{GMa(1-e^2)}, \tag{3.15}$$

where $M = M_1 + M_2$ is the total mass of the binary system. Using relations (3.14) and (3.15), we get

$$v_p = \sqrt{\frac{GM}{a}\frac{1+e}{1-e}}, \quad v_a = \sqrt{\frac{GM}{a}\frac{1-e}{1+e}}. \tag{3.16}$$

If star 1 is the blue straggler that we observe, its pericenter and apocenter velocities are given as

$$v_{1,p} = \frac{M_2}{M} v_p, \quad v_{1,a} = \frac{M_2}{M} v_a. \tag{3.17}$$

Finally, we add these velocities together to obtain the maximum possible amplitude of the RV curve (if the inclination of the system is 90°) as

$$\Delta v_{r,\max,1} = \sqrt{\frac{G\ M_2^2}{a(M_1+M_2)}} \left(\sqrt{\frac{1+e}{1-e}} + \sqrt{\frac{1-e}{1+e}} \right), \tag{3.18}$$

and we obtain v_K for the primary star as

$$v_K = \frac{\Delta v_{r,\max,1}}{2}. \tag{3.19}$$

In case of a non-circular orbit, this does not reproduce the exact shape of the RV curve and is only an approximation. But this is not an issue, since we expect the majority of orbits to be circular after mass transfer due to tidal dissipation.

Inclinations of binary orbits are random, i.e. all inclinations are equally likely (e.g. Gillett, 1988). The vector perpendicular to the orbital plane has an equal chance to point at any unit area of a sphere. The area on the surface of a sphere swept out by a circular strip at inclination i and opening angle di is $2\pi \sin i \, \mathrm{d}i$. The probability density function of isotropic inclination angles is then given by

$$f(i) = \frac{1}{2}\sin(i), \quad 0 \leq i \leq \pi. \tag{3.20}$$

Knowing the probability density function, we can draw random values of i. Lastly, we need to take the orbital phase θ into account. We first take a random number between 0 and 2π, which represents the orbital phase during the first observation θ_i. Now we also need to consider the time-span of observations and the orbital period of the binary. If the period is hundreds of years long, we would not observe a significant change in the RV over a few years. We therefore determine an interval

of orbital phases, which we can observe considering the time-span of observations to be t_{obs}. This interval is determined as

$$\Delta\theta = 2\pi \frac{t_{\rm obs}}{P}. \tag{3.21}$$

We then draw random orbital phases from an interval between θ_i and $\theta_i + \Delta\theta$. Now we have all the tools to make n random measurements of the radial velocity using equation (3.13).

3.3 Isochrone masses

For modeling purposes, we estimate the masses of stars using `PARSEC` isochrones (Bressan et al., 2012). Our first approach is to select isochrones with metallicity closest to the observed star ([Fe/H] within 0.05 dex) and then we calculate the distances to isochrone points from the observed values in both the CMD and the Kiel diagram. We then obtain the stellar mass from the closest grid point and visually check that the closest isochrone point has been chosen. We refer to this way of obtaining the isochrone mass as "the closest point" method.

For a more rigorous approach, we use the maximum likelihood estimation (MLE). Given a set of observables $\boldsymbol{x}$, the likelihood function for the parameter m is given as (Sahlholdt & Lindegren, 2021)

$$L(m|\boldsymbol{x}) = \exp\left[-\frac{1}{2}\sum_i \left(\frac{x_i - X_i(m)}{\sigma_i}\right)^2\right], \tag{3.22}$$

where $\boldsymbol{X}$ is a set of isochrone predictions for the observables, and σ_i is the uncertainty of the observable x_i. We use M_G, $(\mathrm{BP}-\mathrm{RP})_0$, and [Fe/H] as our set of observables. We make an initial selection of points from the isochrone grid based on the uncertainties of the observed quantities. Uncertainty of the apparent G magnitude is given by

$$\sigma_G = \frac{2.5}{\ln 10}\frac{\sigma_{F_G}}{F_G}, \tag{3.23}$$

where F_G is the G-band mean flux and σ_{F_G} is its uncertainty. We can similarly calculate the uncertainty for BP and RP magnitudes. We use the dereddened color from `StarHorse` and it is not straightforward what the uncertainty on that value is. Only percentiles for extinction in the V-band A_V are listed, so as a rough estimate, we assume that the uncertainty σ_{A_V} is the same as uncertainty in the extinction in all Gaia bands. We take

$$\sigma_{A_V} = \frac{1}{2}(A_{V84} - A_{V16}), \tag{3.24}$$

where A_{V84} and A_{V16} are the 84th and 16th percentile values. Similarly for the distance uncertainty from Bailer-Jones et al. (2021), we take

$$\sigma_d = \frac{1}{2}(d_{84} - d_{16}). \tag{3.25}$$

We finally obtain the uncertainties of the absolute magnitude and dereddened color index as

$$\sigma_{M_G} = \sqrt{\sigma_G^2 + \sigma_{A_V}^2 + \left(\frac{5}{\ln 10}\frac{\sigma_d}{d}\right)^2}, \tag{3.26}$$

$$\sigma_{(\mathrm{BP-RP})_0} = \sqrt{\sigma^2_{\mathrm{BP}} + \sigma^2_{\mathrm{RP}} + 2\sigma^2_{A_V}}. \tag{3.27}$$

We then make an initial selection of isochrone points around the observed parameters of the star that are within $\pm 3\sigma_{M_G}$ and $\pm 2\sigma_{(\mathrm{BP-RP})_0}$. When it comes to the metallicity, the isochrone grid has steps of 0.1 dex in [Fe/H]. The [Fe/H] uncertainties determined by APOGEE and GALAH are around 0.02 dex, so we select the set of isochrones that is the closest to the observed value. Within this cube in $M_G - (\mathrm{BP} - \mathrm{RP})_0 -$[Fe/H] space, we calculate the likelihood function for each isochrone grid point. We then select the point with the maximum likelihood and take its mass to be the mass of the observed star.

To estimate the uncertainty, we look at ten points with the largest likelihood, take the maximum mass, subtract the minimum mass, divide by two, and that gives us a range of possible isochrone masses. This is not a rigorous approach to uncertainty determination, but it gives us an idea about the uncertainty between the individual stars in the final sample.

Chapter 4

Results

In this chapter, we summarize the results for stars in the final sample. In Section 4.1, we look at chemical abundances and radial velocity variations determined by spectroscopic surveys, and we also show the isochrone mass estimates. In Section 4.2, we show the results of the population synthesis. We determine the likely formation channels for stars in the final sample, make synthetic radial velocity measurements of the generated binaries, and compare the RV variations between the observed and generated samples. In Section 4.3, we present the results of detailed modeling of formation for two systems for which we have the radial velocity curve.

4.1 Population characteristics

4.1.1 Chemical abundances

Metallicity distribution functions (MDFs) for the final samples are shown in Figure 4.1. Feuillet et al. (2021) show broad MDFs for the accreted populations Gaia-Sausage-Enceladus and Sequoia, and the MDFs of the stars in the APOGEE and GALAH accreted samples are consistent with them. The GALAH non-accreted sample contains some very metal-poor stars with [Fe/H] < -2 dex, and there is also a high peak at [Fe/H] > -1 dex, likely resulting from contamination by stars from the disk.

We look for any patterns in other elemental abundances. Abundance plots for α, Mg, Mn, Ba, Li, and Zn are shown in Figure 4.2 for the GALAH stars. Abundance plots for α, Mg, and Mn for the APOGEE stars are shown in Figure 4.3.

Looking at the α-elements, we see that [α/Fe] is generally lower for the accreted sample. Same applies to [Mg/Fe], since Mg is one of the α-elements. This is in agreement with previous findings that the halo consists of two main populations: high-α and low-α populations (Nissen & Schuster, 2010). There appears to be a large enhancement in [Mg/Fe] for the GALAH sample with [Fe/H] below -2.0 dex. Higher [Mg/Fe] abundance for metal-poor halo stars has been observed (e.g. Roederer et al., 2014).

Manganese is one of the iron-peak elements, which is primarily formed through SNe Ia. We would expect a roughly constant Mn abundance for stars at low metallicity and an increasing trend from [Fe/H] ≈ -1.0, when the delayed SNe Ia start to enrich the interstellar medium in Fe-peak elements (Kobayashi et al., 2006). This is roughly what we see in the stars in our sample but with a large scatter. No

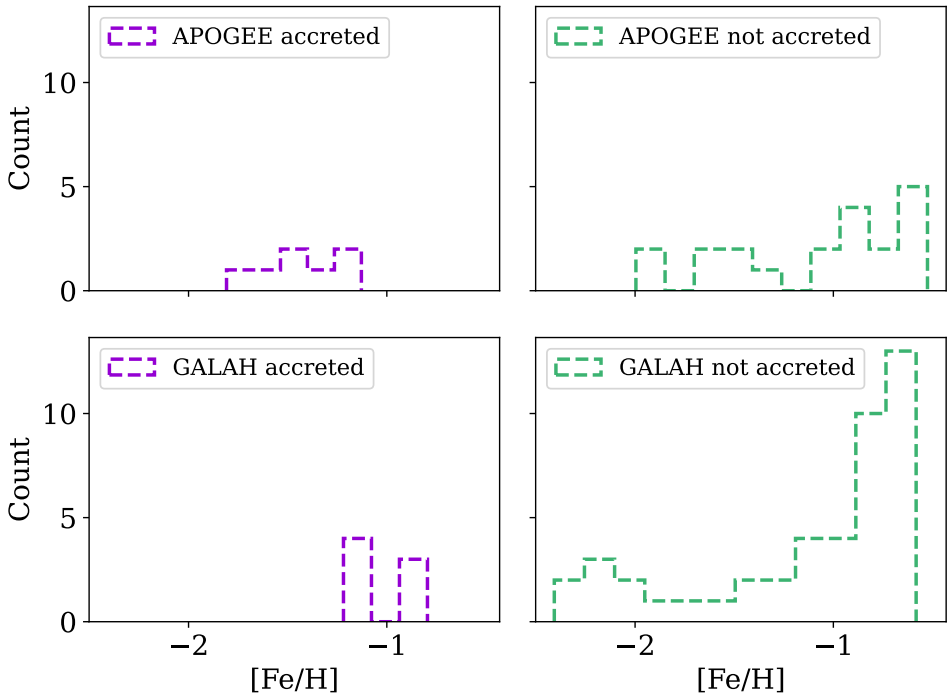

Figure 4.1: Metallicity distribution functions for stars in the final sample.

significant differences are seen between the accreted and non-accreted stars. Large enhancement in [Mn/Fe] for the most metal-poor stars is observed in the GALAH sample. This has not been observed in halo stars (Reggiani et al., 2017), so this could hint towards a pipeline issue.

Looking at the barium abundances, there is one star (04374970-0123263) that has significantly enhanced Ba abundance with [Ba/Fe] $\approx$ 1.5 dex. There is also one more star (15450652-1953387) that seems to be significantly enriched in Ba with [Ba/Fe] $\approx$ 0.88 dex, but this star has the lowest metallicity in our sample, so the value is more uncertain. There are five stars that have slightly enhanced Ba abundance with [Ba/Fe] $>$ 0.2 dex (13152913-1321116, 08160733+1941519, 03163723-5755051, 12283812-0106341 from the non-accreted sample, and 14024428-0929107 from the accreted sample). Higher [Ba/Fe] abundance could indicate that these systems formed via mass transfer from an AGB star.

In the A(Li)$-$[Fe/H] space, most stars have A(Li) $\approx$ 2.2 as has been previously observed in metal-poor stars (Spite & Spite, 1982). These stars are on the cooler side of the lithium dip. In the accreted sample, there are two stars that do not have [Li/Fe] measurements, indicating their depletion in lithium. One of them (22424052-5013383, with $T_{\rm eff}$ = 6369 K and $\log g$ = 3.71) lies on the hotter side of the lithium dip and not in the dip (see Figure 1.3 for reference), so the absence of lithium measurement could hint towards mass transfer evolution of this system. The other system (14024428-0929107, with $T_{\rm eff}$ = 5915 K and $\log g$ = 3.84) lies in the region of the lithium dip, so the absence of the lithium measurement does not necessarily mean that this system went through mass transfer. The one star from the accreted sample having lower Li abundance than the rest (05000611-6745566, with $T_{\rm eff}$ = 6094 K and $\log g$ = 4.01) is around the boundary on the cooler side of the lithium dip. Most of the stars with [Fe/H]<-1.0 dex from the non-accreted sample lie along the Spite plateau value of A(Li) $\approx$ 2.2. One metal-poor star (16100596-3054088) shows

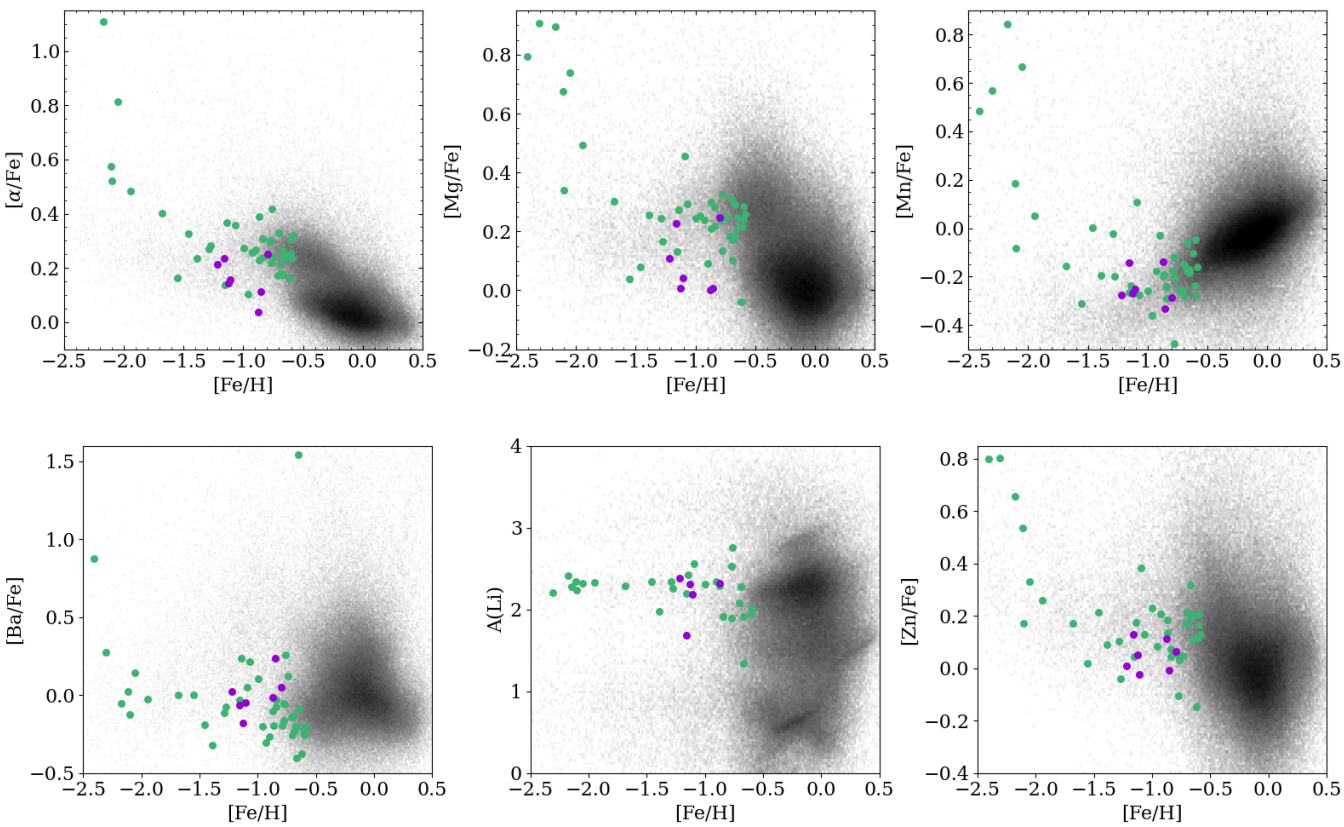

Figure 4.2: [X/Fe] abundances for α, Mg, Mn, Ba, and Zn for the GALAH stars. Lithium abundance is shown as A(Li). Green points show the non-accreted sample and purple points show the accreted sample. Black points in the background show the entire GALAH dataset.

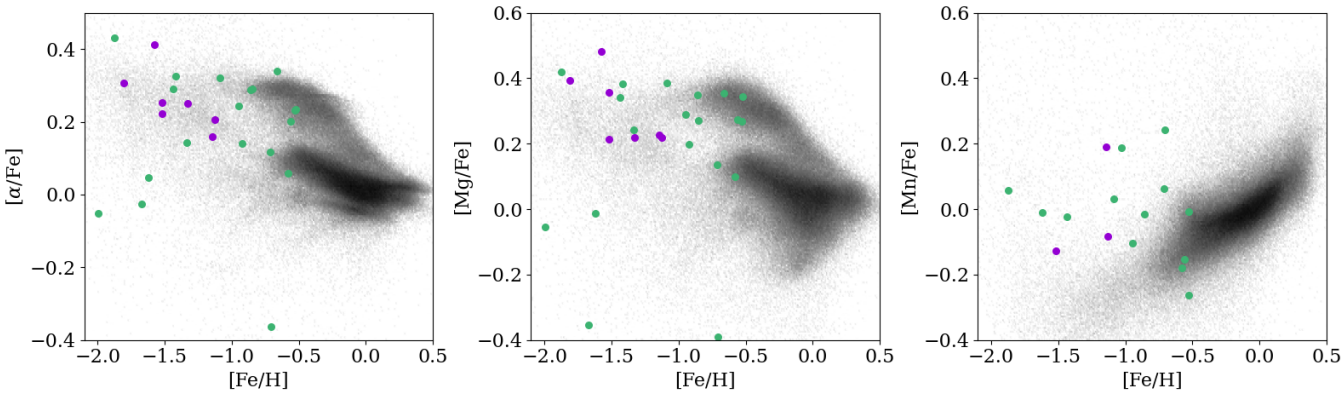

Figure 4.3: [X/Fe] abundances for α, Mg, and Mn for the APOGEE stars. Green points show the non-accreted sample and purple points show the accreted sample. Black points in the background show the entire APOGEE dataset.

minor lithium depletion.

The production of zinc depends on metallicity. At higher metallicity ([Fe/H] $>$ -0.7 dex), both ^{66}Zn and ^{68}Zn are produced during He and C burning. At lower metallicity, only ^{64}Zn is synthesized in the deep complete Si-burning region and mixing into the ejecta is required for enough amount to be ejected (Kobayashi et al.,

2006). So we expect [Zn/Fe] to be roughly constant until [Fe/H] ≈ -1.5 dex, when [Zn/Fe] starts slowly rising due to the metallicity effect, and the abundance starts dropping after [Fe/H] ≈ -1 due to SNe Ia, in which heavier iron-peak element than Co (that includes Zn) are underproduced (Kobayashi et al., 2020). The [Zn/Fe] abundance is higher for stars with [Fe/H] below -2.0 dex. These measurements might not be so unrealistic as [Zn/Fe] enhancement in low metallicity stars has been observed (e.g. Reggiani et al., 2017). Large energies of hypernovae explosions present in the early galaxy might be able to reproduce this high Zn abundance observed in extremely metal-poor halo stars (Umeda & Nomoto, 2002).

4.1.2 Radial velocity variations

Most of the stars show variability in radial velocity. Out of the 79 stars in the final sample, four (all in the GALAH non-accreted sample) only have a single radial velocity measurement; the rest have at least two. We use all RV measurements to determine what the maximum change in the RV is for each star, therefore estimating the amplitude of the RV curve. We take slightly different approaches between the APOGEE and GALAH datasets. The APOGEE dataset contains RV measurements for each individual visit, so we take all these RV measurements and one RV measurement from Gaia DR3. In case of GALAH, we do not have access to the RV measurements from individual visits, and only one RV value is available. We also use the RV value from Gaia DR2 or Gaia DR3, and we never use both for a single star. For each star, we take the maximum value of RV, subtract the minimum value from it, and this determines the maximum detected RV variation Δv_r. This value for each star is plotted in Figure 4.4 as a function of metallicity.

There are three stars with $\Delta v_r > 50$ km/s, which is higher than we would expect for BSSs, so we look into each system individually. One star (2M16024225-2029174) comes from the accreted sample. For this star, we conclude that the

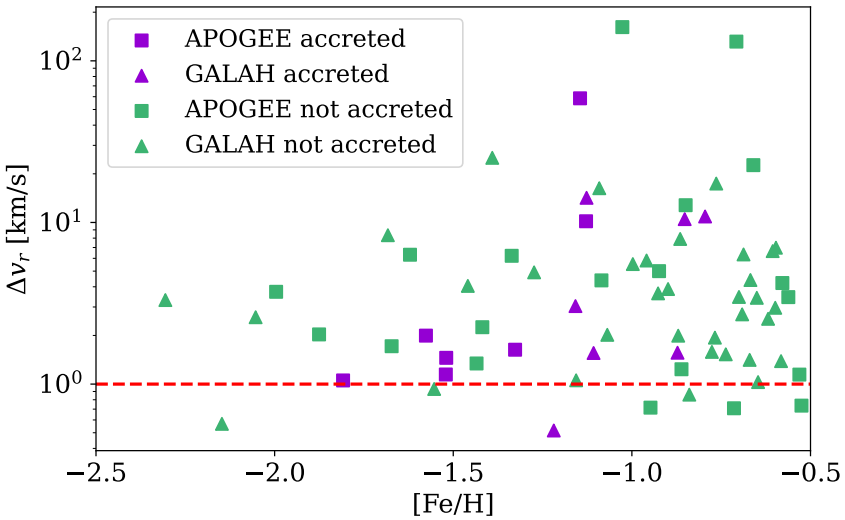

Figure 4.4: Maximum detected radial velocity variation for each star in the final sample as a function of metallicity. The red horizontal line at 1 km/s shows the typical precision of RV measurements, stars with $\Delta v_r > 1$ km/s are likely binaries; 58 stars are above this threshold, 17 are below, and 4 stars are not included (they have only one RV measurement).

RV measurements are reliable. It was observed five times by APOGEE, and the radial velocities vary between 215 and 273 km/s, while the measurement from Gaia is 258 km/s. These values are reasonable given that the system is an eclipsing binary consisting of a dwarf and a sub-giant star (Maxted & Hutcheon, 2018). The inclination of the system is very close to 90°, so the maximum possible RV variation is observed. The other two stars (2M05513901-5951092 and 2M07250746-6745394) do not seem as reliable. They have spectra with broad lines and even some emission features. They might be rapidly rotating stars and/or have companions. They were both observed only once as part of the TeskeVanSaders_18a program, which targets mainly astroseismically active stars also observed by TESS. For both stars, radial velocities from Gaia are consistent between the two data releases (with large uncertainties suggesting RV variability) and the RV measured by APOGEE is more than 100 km/s greater than these values, so the measurements might be wrong. We keep these stars in the final sample as they still passed all of our selection criteria, but we need to be careful when drawing any conclusions using these stars.

4.1.3 Isochrone masses

We first determine the isochrone masses by using "the closest point" method as described in Section 3.3. We do this both in the color-magnitude space and in the $T_{\rm eff} - \log g$ space. The results are shown in Figure 4.5. We see that fitting in the CMD leads to systematically higher mass estimates. There is one star that really stands out, star labeled as 36 (18313894-5427314) in the GALAH non-accreted sample. This star shows a very large difference in the mass determined in the two planes. After looking at the parameters of the star, we determine that it is actually a giant that made it into the final selection. Its effective temperature is relatively low ($T_{\rm eff} = 5121$ K) and its surface gravity is the lowest out of all the stars in the sample ($\log g = 2.87$). In the CMD, it is very close to the giant branch (see Figure 2.6), and it is likely that its dereddened color has a large uncertainty, and it ended up in our CMD selection cut.

Systematically higher isochrone masses are consistent with the fact that the effective temperature of stars hotter than 6000 K is underestimated in GALAH (Buder et al., 2021). This is most likely the case for APOGEE stars as well. Using photometry therefore seems more reliable when it comes to the determination of masses, so we make the final mass estimates in the CMD using MLE as described in Section 3.3. We take the mass of the most likely isochrone point to be the stellar mass, and we estimate the uncertainty by looking at the range of masses in the ten most likely isochrone points. The final masses of stars are shown in Figure 4.6. The isochrone masses for each star are listed in Appendix A.

4.2 Population synthesis results

We create a sample of binaries as described in Section 3.1.3. We generate a large number of blue stragglers using BSE, and see where they lie in the CMD. We then construct a box in the CMD around each star in the final sample and look at the formation histories of the generated blue stragglers. This allows us to determine what the most likely formation channel is for each star in the final sample, even if we do not have a lot of information about the system.

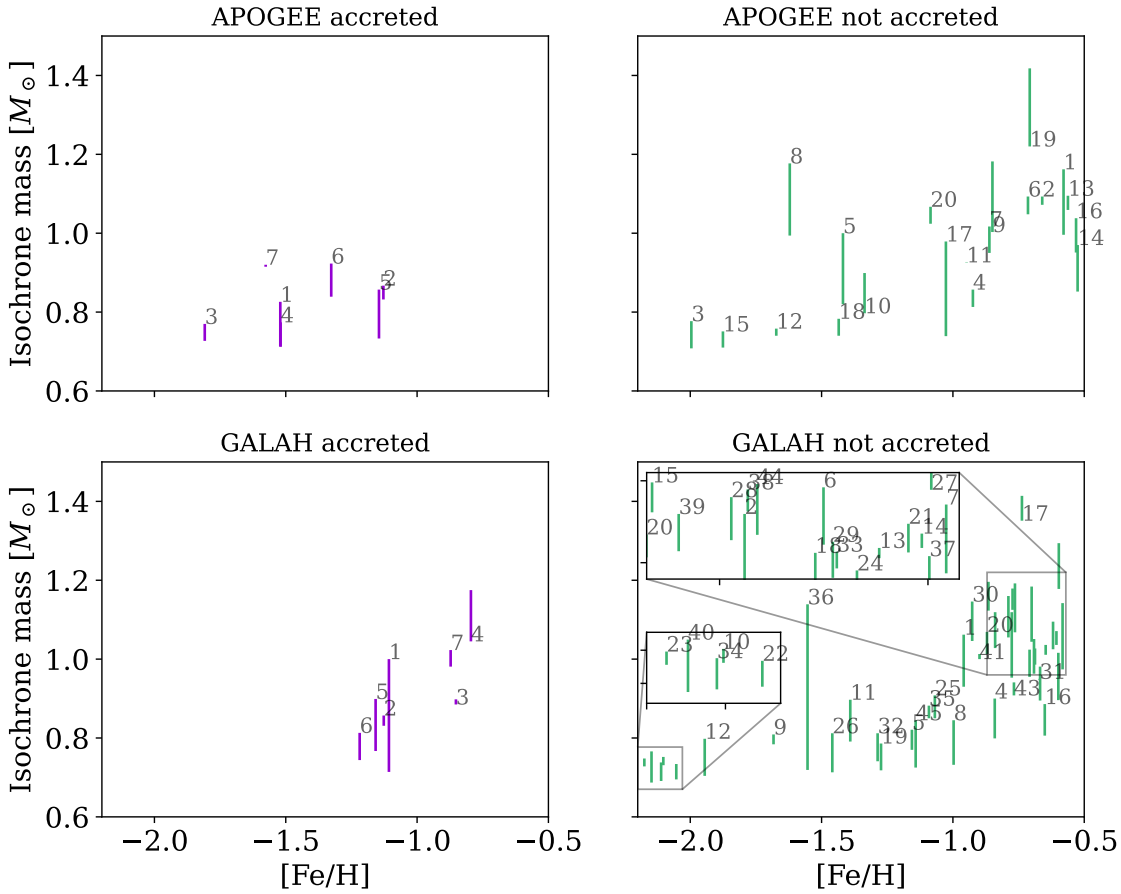

Figure 4.5: Masses of stars in the final sample determined through finding the closest isochrone point to the observed star. Each vertical line represents one star. Lines are numbered and the side on which the number is, represents the mass estimate obtained through fitting in the CMD. The opposite side of the line represents the estimate obtained in the $T_{\rm eff} - \log g$ space. The vast majority of stars have numbers on top of the lines, showing that using spectroscopically determined parameters results in underestimation of the mass.

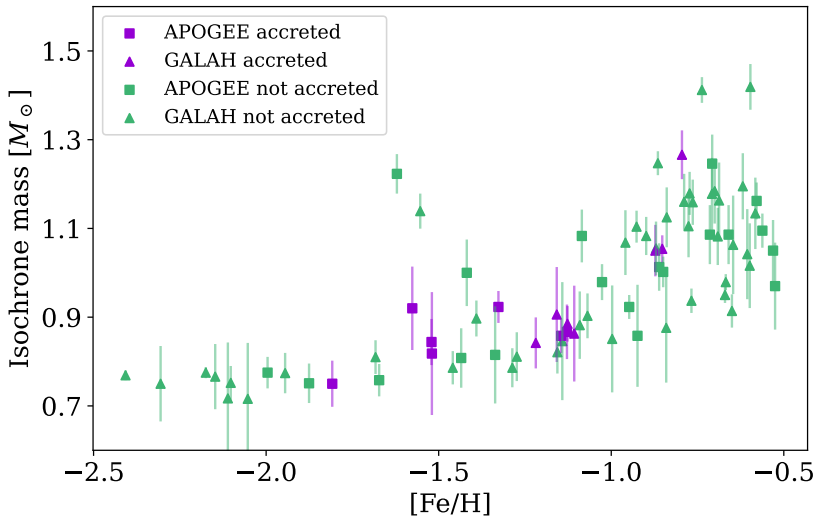

Figure 4.6: Isochrone masses of stars in the final sample, determined using MLE.

We generate 250000 binaries with metallicity of $Z = 0.002$. We limit ourselves in the initial parameter space space in order to create as many blue stragglers as possible in the least amount of computing time. We draw the initial masses of the primary stars only between 0.75 $M_\odot$ and 10 $M_\odot$. The lower limit comes from the fact that we need the primary to evolve in order to form a BSS. Given that the turn-off mass of a halo-like population (10 Gyr old and [Fe/H] $= -1$) is $M_{\rm TO} \approx 0.85\ M_\odot$, this lower limit is actually quite conservative. Upper limit comes from the fact that more massive stars are also much more rare. We then also limit the initial semi-major axis between 3 $R_\odot$ and 100 au. Stars with the initial separation lower than the lower limit result almost immediately in a merger, so this does not result in a BSS. The upper limit is used because we need the stars to interact in order to form a BSS. If they are too far from each other, they just evolve as single stars without ever interacting. Figure 4.7 shows that this region of initial parameter space contains the largest number of blue stragglers.

After evolving all the binaries for 10 Gyr, we access the evolution log of each one and use those that go through a blue straggler phase for further analysis, and only select those that have not evolved into RGB stars yet. This gives us the total of 3916 BSSs. To obtain the evolution history of each BSS, we look at what evolutionary stage was the primary star on when it filled its Roche lobe or whether the BSS formed through a merger. As a reminder, we distinguish between the following cases: type A (donor is a MS star), type B (donor is a RGB star), type C (donor is an AGB star), and type D (wind accretion). There is also a special case when the Roche lobe filling star is in the Hertzsprung gap and we refer to this case as HG. We also distinguish between cases when only type B or type C mass transfer occurs, and between the case when both types occur during the evolution of a binary. We refer to this case as type B+C.

We find: 8 cases of type A mass transfer that ends in a merger, 22 cases of type A mass transfer when the binary survives, 120 cases when the donor fills its Roche lobe while being in the Hertzsprung gap, 2418 cases of pure type B mass transfer, 477 cases when type B mass transfer is followed by type C mass transfer, 274 cases of pure type C mass transfer, and 602 cases of type D mass transfer. It is important to mention that some of the type A, HG, and type B mass transfers overlap, but we do not differentiate between these cases as the number of type A and HG mass transfer cases are small compared to the other ones. Figure 4.8 shows the mass of the BSSs at 10 Gyr as a function of the orbital period of the binary. The points

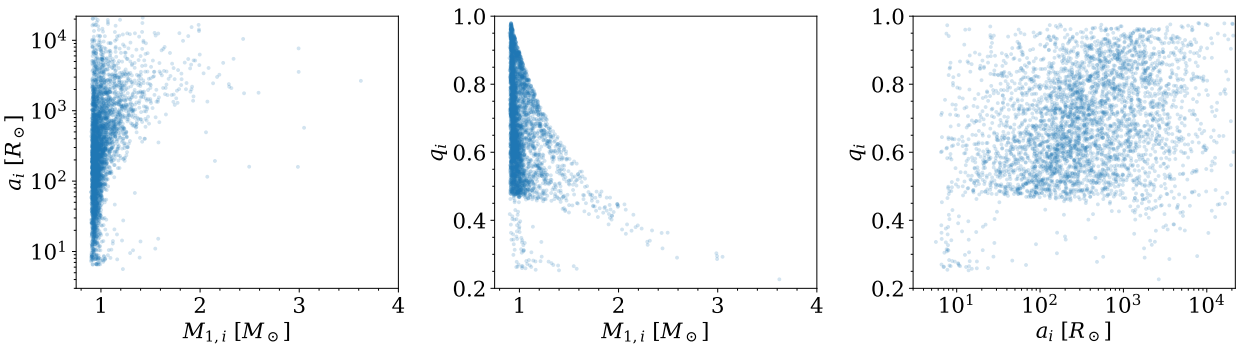

Figure 4.7: Initial parameters (initial mass of the primary $M_{1,i}$, mass ratio q_i, and separation a_i) plotted as functions of each other for the population of model BSSs.

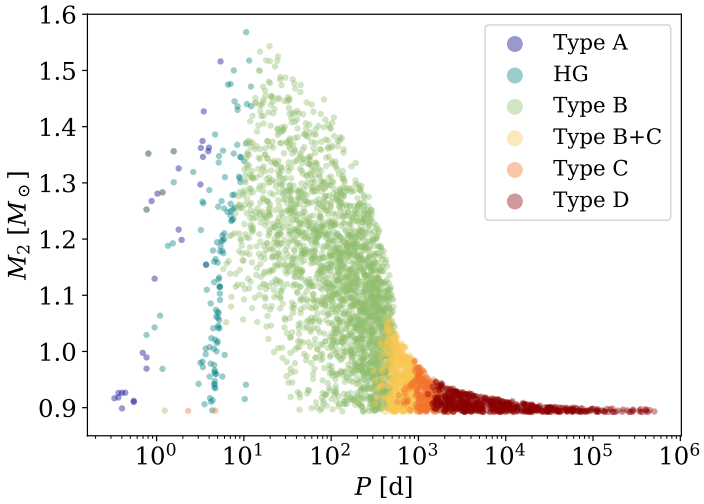

Figure 4.8: Mass of the generated BSSs at 10 Gyr as a function of the orbital period of the binary. The points are colored by the formation channel.

are colored by the formation channel, and the plot shows a correlation between the formation channel and the position in this space. The dominant formation channels changes as we look at BSSs with different orbital periods. We also see that the most massive BSSs ($M > 1.1\ M_\odot$) form primarily through type B mass transfer when the companion evolves off the MS and becomes a red giant.

4.2.1 Formation channels

Having the formation histories of the generated sample, we construct a box in the CMD around each star in the final sample. We increase the size of the box in steps of 0.0025 in $(\mathrm{BP} - \mathrm{RP})_0$ and 0.013 in M_G until each box contains at least 100 model BSSs. For each star, we then determine what percentage of generated BSSs formed through each formation channel. The results for each star in the final sample are summarized in Appendix A. We then sum up the number of cases for each type of mass transfer and divide our sample into metallicity bins. The resulting histograms are shown in Figure 4.9.

4.2.2 Synthetic radial velocity measurements

Part of the analysis is also trying to recreate the measured radial velocity variations shown in Figure 4.4. As previously, we make a box in the CMD around each star containing 100 generated BSSs. If a star has n radial velocity measurements, then we make n number of measurements for each generated BSSs in the box, following the procedure described in Section 3.2. We then determine the observed variation in RV for each generated binary and obtain the final synthetic Δv_r of our model as the mean of all values in the selected box, and the uncertainty as the standard deviation of the values. We make these measurements for the observation periods of 1 and 10 yr. The results as well as the residuals (value from the model subtracted from the observed value) are shown in Figure 4.10. There seems to be a systematic offset between the model and observations and the model overestimates the variation in radial velocity. This offset is smaller when considering a shorter observation period

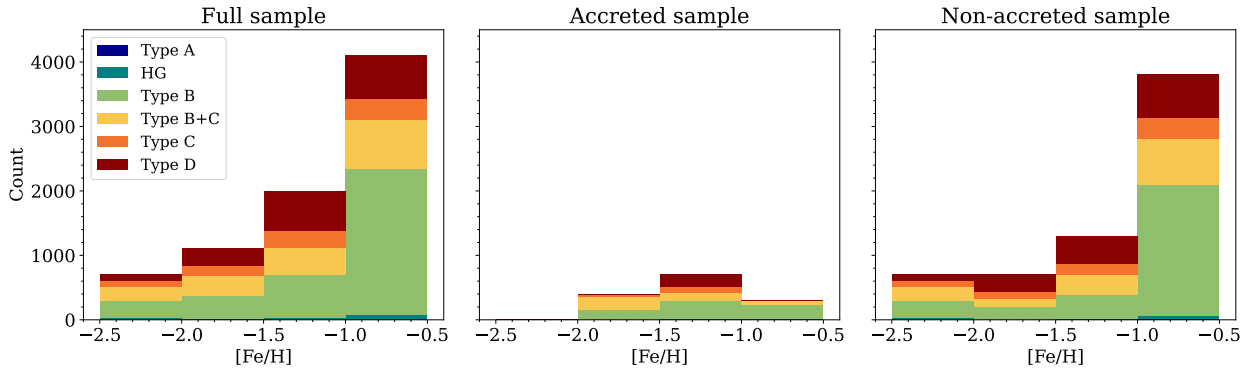

Figure 4.9: Histograms of the formation channels for the full, accreted, and non-accreted samples. A box was made around each star in the final sample that included 100 generated BSSs. The histograms show the formation channel of these generated binaries, so each observed BSS appears 100 times in the histogram. Type B mass transfer dominates for the highest metallicity bin.

of 1 year. The synthetic BSE Δv_r values, considering the observation period of 1 year, are shown in Appendix A for each star in the final sample.

4.3 Selected individual systems

4.3.1 2M16355860+4551590 (APOGEE accreted sample)

This star has been mentioned in a lot of previous studies, is a known halo BSS, and is classified as a single-lined spectroscopic binary, consistent with having a white dwarf companion (Carney et al., 2001). It is lithium deficient (Ryan et al., 2001), which is an indication that the system has been through mass transfer. Carney et al. (2001) measured the radial velocity curve of the binary and concluded that

$$P = 167.54 \text{ d}, \quad M_1 = 0.87\ M_\odot, \quad M_{2,\text{min}} = 0.5\ M_\odot, \quad e = 0.15.$$

Having these constraints, we can make a detailed model for the formation of this system. We use the least-squares fitting method described in Section 3.1.2 to find the best fit to the observables: current orbital period of the binary P and the mass of the BSS M_2. However, we have one more unknown parameter, which is the mass of the secondary M_1, which was initially the primary (before the mass ratio turned after mass transfer). So the procedure is as follows, we fix the initial mass of the primary and make a grid of points in the $P_i - M_{2,i}$ space (initial orbital period vs. the initial mass of the secondary). We use the metallicity $Z = 0.002$ and the initial eccentricity $e_i = 0.5$. For each point in the grid, we run BSE and if the evolution results in a BSS, we take its mass and orbital period, and compare it with the observed value by calculating the value of χ^2-function. We first do a broad search in the parameter space to see where the solutions lie. We then refine the grid to zoom in on the solutions. We use the `scipy.optimize.brute` function, which calculates χ^2 at each point of the grid. After finding the minimum value, it calls the `scipy.optimize.fmin` function, and it uses the best fit grid point as the initial guess for the fit. Figure 4.11 shows that visually. It demonstrates the complexity of this parameter space and the degeneracy between the different types of mass transfer as we can recreate the system through different pathways.

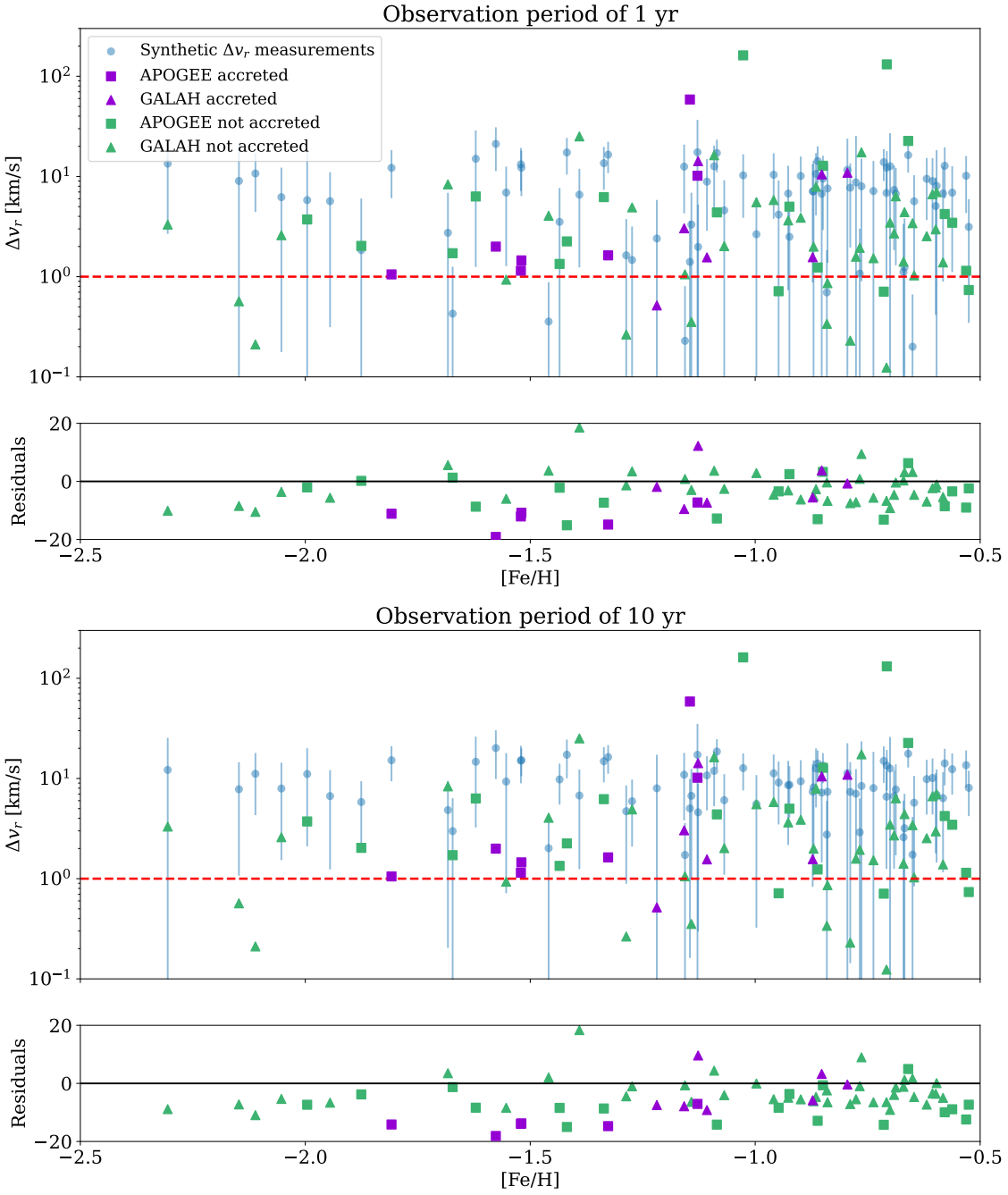

Figure 4.10: RV variations from synthetic RV measurements plotted over the RV variations of the final sample. Top panels show results for the considered observation time-span of 1 yr and the bottom panels for the observation time-span of 10 yr. The systematic offset between models and observations is smaller for the shorter observation period. Red horizontal line indicates the typical precision of the RV measurements, any star with Δv_r above this threshold is likely a binary.

We find solutions for 3 different fixed initial masses of the primary. Each case leads to a different evolution and we look at solutions in each branch. The results are shown in Table 4.1, where we also include the maximum possible RV amplitude $\Delta v_{r,\max}$ (if the inclination of the system is 90°), time when the BSS phase begins $t_{0,\mathrm{BSS}}$ which needs to be consistent with the age of the halo, and lastly the lifetime on the main sequence τ_{MS} for the BSS. This lifetime is a good indication how likely

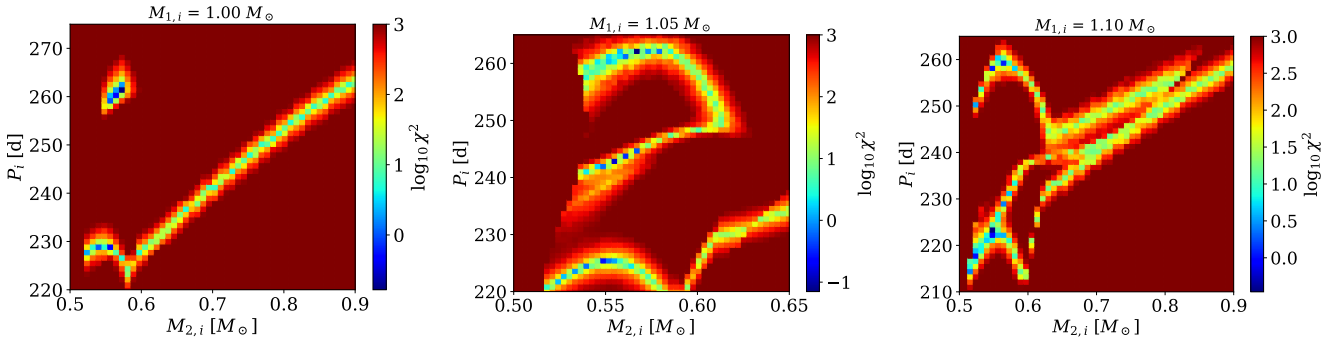

Figure 4.11: Visualization of the initial parameter space for 2M16355860+4551590. We fix the initial mass of the primary (indicated above each plot), and search the $P_i - M_{2,i}$ parameter space (initial orbital period vs. the initial mass of the secondary) to find the best fit given the observables (mass of the BSS and the orbital period). Regions with the lowest $\log_{10}\chi^2$ correspond to the best fit models. Plots show that the observed system can be recreated using multiple formation channels.

Table 4.1: Results of the fitting for 2M16355860+4551590. We show which type of mass transfer occurs during the evolution of the binary, the initial masses for the donor and the accretor, and the initial orbital period of the system. We list some parameters of the system during the BSS phase: mass of the former primary M_1, mass of the BSS M_2, orbital period P, separation a, maximum amplitude of the radial velocity curve $\Delta v_{r,\max}$, time when the BSS phase starts $t_{0,\mathrm{BSS}}$, and lifetime of the BSS on the main sequence τ_{MS}.

Initial parameters				BSE outcome during BSS phase						
Mass transfer	M_1 [$M_\odot$]	M_2 [$M_\odot$]	P [d]	M_1 [$M_\odot$]	M_2 [$M_\odot$]	P [d]	a [$R_\odot$]	$\Delta v_{r,\max}$ [km/s]	$t_{0,\mathrm{BSS}}$ Myr	τ_{MS} Myr
B+C	1.00	0.570	260.1	0.529	0.860	168.0	143.0	32.8	10706	5142
B+C	1.05	0.567	262.1	0.532	0.86	168.0	143.1	32.9	10702	4397
B	1.05	0.543	224.9	0.494	0.872	168.0	142.2	31.0	10229	4509
B	1.05	0.560	243.6	0.527	0.869	168.0	143.3	32.6	10429	4332
B	1.10	0.548	223.2	0.502	0.895	168.0	143.2	31.0	9378	3835
B+C	1.10	0.565	259.1	0.533	0.884	168.0	143.7	32.6	9730	3839

we are to observe the system; if it is only a few million years long, then we are very unlikely to observe the system today. We do not list any uncertainties on these values as we are only trying to show that we can indeed recreate this system through different formation channels.

We can recreate the observed mass and orbital period very accurately, but we cannot explain the observed eccentricity ($e = 0.15$). In our models, the system circularizes even before the primary star fills its Roche lobe. This is a known issue in binary star evolution as some stars that seem to have gone through mass transfer also have some orbital eccentricity (e.g. North et al., 2000).

4.3.2 08160733+1941519 (GALAH non-accreted sample)

This is another previously studied BSS that is classified as a single-lined spectroscopic binary. Pourbaix et al. (2004) find

$$P = 60.62 \text{ d}, \quad e = 0.46.$$

Following the procedure explained in the previous subsection, we explore the parameter space to find the best fit to the currently observed orbital period and the isochrone mass of the BSS. We use the metallicity $Z = 0.0001$ and initial eccentricity $e_i = 0.5$. We try five different fixed initial masses of the primary and in all cases, only one branch is visible in the parameter space (Figure 4.12). The results are summarized in Table 4.2.

We can recreate the system only through mass transfer from a red giant, but the results are not convincing. Using the lowest initial mass of the primary best recreates the observed mass of the BSS, but the blue straggler phase starts only 17.6 Gyr after the beginning of its evolution. On the other hand, using higher initial mass of the primary results in a beginning of the blue straggler phase that is consistent with the age of the Galactic halo, but the formed BSS is much more massive than the isochrone mass suggests. We are also unable to recreate the high eccentricity observed in this system due to the limitations of the code, which we discuss in the next chapter.

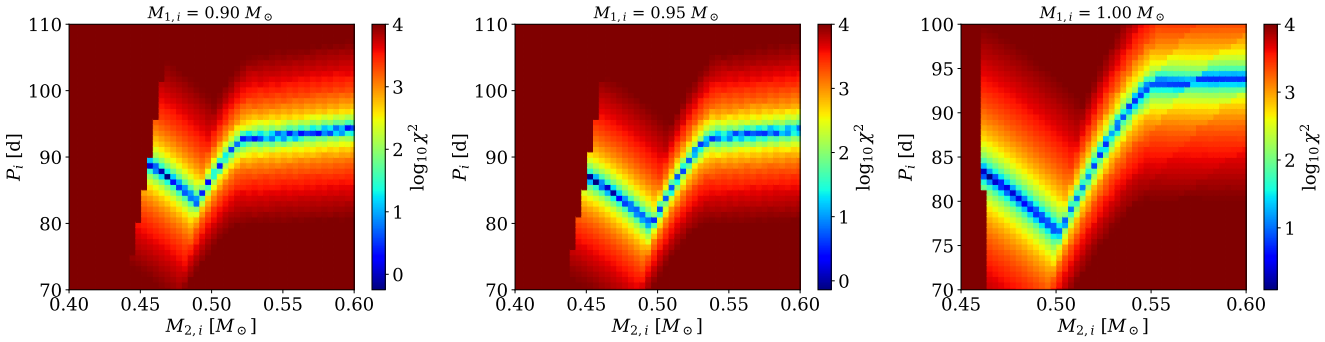

Figure 4.12: Visualization of the initial parameter space for 08160733+1941519. See Figure 4.11 for description.

Table 4.2: Results of the fitting for 08160733+1941519. Columns are the same as in Table 4.1.

Initial parameters				BSE outcome during BSS phase						
Mass transfer	M_1 [$M_\odot$]	M_2 [$M_\odot$]	P [d]	M_1 [$M_\odot$]	M_2 [$M_\odot$]	P [d]	a [$R_\odot$]	$\Delta v_{r,\max}$ [km/s]	$t_{0,\text{BSS}}$ Myr	τ_{MS} Myr
B	0.85	0.45	92.0	0.43	0.75	60.6	68.6	41.5	17561	8341
B	0.90	0.45	90.1	0.43	0.75	60.6	68.6	41.6	17813	6994
B	0.95	0.45	87.2	0.43	0.78	60.6	69.2	40.8	14981	6086
B	1.00	0.46	83.3	0.43	0.85	60.6	70.4	39.3	10942	5187
B	1.05	0.49	76.8	0.42	0.97	60.6	72.4	36.6	6697	4755

Chapter 5

Discussion

5.1 Population characteristics

The APOGEE and GALAH surveys have data for over 1.3 million stars. Despite our rather generous selection criteria, we only end up with a small sample of blue stragglers. This shows that looking for these intrinsically rare objects in populations with low stellar number density, like the field of the Galactic halo, requires a large amount of data. Selection functions of the surveys play a big role in the size of the final sample. APOGEE targeted mostly giants, and with its strict color cut, it is not a surprise that we end up with a smaller sample of blue stragglers compared to GALAH.

It is unclear how mass transfer affects certain chemical abundances, but since the abundances of Mg, Mn, Zn of the accreted population are consistent with what has been measured in the accreted halo stars (Buder et al., 2021) and the massive Milky Way satellites (Hasselquist et al., 2021), it seems like these abundances remain mostly unaffected in post-mass-transfer systems. This is also expected theoretically, since nuclear burning should not affect the abundances of elements this heavy. We know that this is not the case for Ba, Li, C, N, and O abundances, which can get significantly altered during mass transfer. We indeed see stars enhanced in Ba and stars depleted in Li, the formation of which we can explain with our BSE models. We have the abundances for C, N, and O for the APOGEE stars, which we inspected. However, they have much higher uncertainties than typical and we therefore do not draw any conclusions from them.

In the GALAH non-accreted sample, the abundances of Mg, Mn, and Zn significantly increase towards the lowest metallicities. The high [Zn/Fe] abundance for the most metal-poor stars can be physically explained by the enrichment from hypernovae (Kobayashi et al., 2006). High [Mg/Fe] abundance has been observed in metal-poor halo stars (Reggiani et al., 2017), but not as high as we see in our sample. Increased [Mg/Fe] and [Mn/Fe] for the most metal-poor stars in our sample is difficult to explain. It could be caused by the fact that we are looking at relatively hot stars, which are also metal-poor. Both of these effects make the spectral lines weaker and the measurements less reliable. We do not see such features in the APOGEE sample, but it does not have any stars with [Fe/H] < -2.0 dex.

The vast majority of stars in the final sample show radial velocity variation ($\Delta v_r > 1$ km/s), which is a good indication that they are in a binary system. We are expecting to look at stars that underwent mass transfer, so this suggests that a

large fraction of our final sample includes genuine BSSs. Due to the small sample size and complexity of the selection function for both spectroscopic surveys, we are unable to make any conclusions about the differences in binary fractions between the accreted and non-accreted samples.

Determination of the isochrone masses shows a systematic underestimation when fitting in the $T_{\rm eff} - \log g$ space, compared to the color−magnitude space. This is in agreement with the claim from Buder et al. (2021) that the effective temperature of stars hotter than 6000 K is underestimated in the GALAH dataset. This seems to be true for the APOGEE stars as well. Our way of determining uncertainties gives us an easy way to quantify and compare the uncertainty in mass between individual stars in the final sample. Obtaining more robust uncertainty estimates would require a more complex analysis including the IMF, implementing the evolutionary stages of stars, isochrone uncertainties, and so on.

5.2 Population synthesis

Generating a population of different metallicity would change the results of our population synthesis, but we decide to use $Z = 0.002$ ([Fe/H] ≈ -1 dex) as a 10 Gyr isochrone of this metallicity matches the halo population very well. This metallicity is also close to the median value of the final sample ([Fe/H] $= -0.95$ dex). We investigated the difference between 9, 10, and 11 Gyr isochrones implemented in BSE. The differences were minor, so we would not expect a significant difference in our results if we evolved the binaries for a slightly different amount of time.

Looking at the formation channels of the generated sample of blue stragglers (Figure 4.8), we see a correlation between the mass of the blue straggler, orbital period of the binary, and the formation channel. The more massive BSSs ($M > 1.1\ M_\odot$) form almost exclusively through mass transfer from a RGB star. It is the most efficient type of mass transfer, which can end up forming a BSS with a mass of almost 1.6 $M_\odot$ (given our metallicity and age assumptions). On the other end, the least massive BSSs form primarily through wind accretion. Looking at the orbital periods, the dominant type of mass transfer transitions from B ($10 < P$[d] < 400, donor was an RGB star) to B+C ($400 < P$[d] < 900, mass transfer occurred when the donor was an RGB star as well as later when it was an AGB star), C ($900 < P$[d] < 1500, donor was an AGB star), and finally D (mass accreted from stellar winds) for the binaries with the longest orbital periods (P[d] > 1500).

After obtaining the formation channels for the stars in our sample using the generated BSSs (Figure 4.9), we see that type B mass transfer is the dominant channel of formation for the highest metallicity bin. This makes sense since this bin also contains the most massive stars, and as we previously said, the most massive BSSs ($M > 1.1\ M_\odot$) form primarily through type B mass transfer. All formation channels are present throughout the entire metallicity range. Accreted and non-accreted samples show different ratios between the different types of mass transfer, but they are also not inconsistent with being the same, since the size of our sample is quite limiting. We would not expect a significant difference in the formation channels between the accreted and non-accreted samples, since binary star evolution should proceed in the same way for both populations.

Synthetic Δv_r measurements (Figure 4.10) show a slight offset from the observed values. The length of the observation period is affecting the results to some extent.

With longer observation period of ten years, Δv_r also gets greater as we get more complete information about the amplitude of the radial velocity curve, especially for the longer period binaries. The observation period of one year makes the offset smaller. This value is reasonable for the APOGEE RV measurements, since a lot of stars from the APOGEE sample have a few RV measurements in a timespan of days or weeks and a few follow-up observations one year later. It is more unclear how the Gaia RV measurements affect the results as those do not have a clearly defined time of observation. We however think that one and ten year timespan of observations provide a reasonable lower and upper limit. The upper limit of ten years comes from the fact that APOGEE operated for approximately ten years (between 2011 and 2021) and Gaia has been operating for almost ten years (since 2014). A small offset is visible even for the shorter observation period. This could be explained by taking eccentricity of the systems into account: in very eccentric orbits, maximum Δv_r would be greater than in circular orbits, but since the star spends the majority of time closer to the apocenter of the orbit, where it moves slower, the average Δv_r will decrease. In Figure 4.10, this would push the synthetic values lower, explaining the offset between models and observations.

5.3 Individual systems

Looking at stars in the selected region of the CMD inevitably results in finding some peculiar systems, like an eclipsing binary (2M16024225-2029174), star that likely has a wrong RV measurement (2M05513901-5951092), and a double-lined spectroscopic binary (16100596-3054088). We are able to show a more detailed analysis of the formation channel for two BSSs that are classified as single-lined spectroscopic binaries with radial velocity curves measured (2M16355860+4551590 and 08160733+1941519). For the star 2M16355860+4551590, we find that the BSS can be created through type B as well as type B combined with type C mass transfer. Its deficiency in lithium (Ryan et al., 2001) suggests that this system has evolved through mass transfer. However, we do not have the barium abundance for this star, which would help us better constrain the formation channel and tell us whether type C mass transfer is more likely.

For the star 08160733+1941519, we find that we are only able to recreate it through type B mass transfer. However, this system has normal Li abundance and is slightly enriched in Ba. The high eccentricity of this system ($e = 0.48$) also suggests that this system might not have gone through mass transfer. Wind accretion scenario could explain the slight enrichment in Ba and higher eccentricity, but is not consistent with the short orbital period of the binary ($P = 60.6$ d). The formation of this system is therefore quite puzzling and its evolution could involve a third star. We are not considering triple systems in this work, but BSSs are expected to form also in hierarchical triple systems due to the Kozai mechanism and tidal friction, where the two inner stars merge into a BSS, which then forms a binary with the outer star. The orbital period of BSSs formed this way are expected to be longer ($P > 700$ d) than observed in this system (Perets & Fabrycky, 2009).

The higher eccentricity in post-mass-transfer systems is an ongoing problem in binary star evolution. The physics that would allow mass transfer in eccentric binary systems is not included in BSE, and this work provides further evidence that a different mechanism is needed to explain these eccentricities in BSSs. We made an

attempt to lower the circularization effects by implementing the prescription for equilibrium tides by Preece et al. (2022), which lowers the strength of tidal dissipation. This however does not reproduce the eccentricity observed in post-mass-transfer systems. We could use a more complex stellar evolution code and SPH simulations to follow the transfer of mass and angular momentum in the mass-transfer binary. This is not a trivial task, but it could help us better understand the cause of this problem. Different mechanisms causing eccentricity excitation have been proposed in previous studies. Binary stars might undergo these eccentricity excitations due to dynamical perturbations caused by passing stars (Winter & Clarke, 2023), but it is unclear whether this could commonly happen in the open field where dynamical encounters with other stars are quite rare. Other proposed mechanisms include Lindblad resonances in circumbinary disks (Dermine et al., 2013), tidally enhanced model of mass loss (Bonačić Marinović et al., 2008), and white-dwarf kicks (Izzard et al., 2010).

Looking at the results for individual systems, for which we do not have the RV curve, there are a few systems worth mentioning. Starting with the GALAH accreted sample; the star 22424052-5013383 has slight barium enhancement ([Ba/Fe] ≈ 0.25), no lithium detected and it is relatively massive ($M = 1.27\ M_{\odot}$). The measured Δv_r is consistent with the models, which predict that this system could have only formed through type B mass transfer. Putting these findings together, it is very likely that this system contains a helium white dwarf and has evolved via mass transfer from a red giant star. The GALAH non-accreted sample contains two stars with very high Ba abundance. The star 15450652-1953387 has [Ba/Fe] = 0.88, no lithium detected, and its relatively low mass ($M = 0.77\ M_{\odot}$) also suggests that this star might have formed through type C or B+C mass transfer. It unfortunately has only one RV measurement, so we have no estimate of Δv_r for this star. The star 04374970-0123263 shows the highest Ba abundance in our sample ([Ba/Fe] = 1.54) and it also does not have lithium detected. Its small Δv_r is consistent with the model, which predicts that this system formed through mass transfer from an AGB star or through wind accretion. The star 12283812-0106341 shows that the slight Ba enhancement ([Ba/Fe] ≈ 0.25) does not necessarily mean that the system has evolved through mass transfer from an AGB star or wind accretion scenario. Despite its slight Ba enhancement, the system is not consistent with type C or D formation channel due to its high RV variation ($\Delta v_r = 17.4$ km/s) and its higher mass ($M = 1.16\ M_{\odot}$).

5.4 Limitations and future prospects

BSE has a lot of limitations as it is not fully resolving the individual stars, but it allows us to quickly generate a large sample of BSSs and successfully recreate some of the observed systems. Implementing new analytical formulae describing mass transfer in eccentric systems would improve the results. Some of the degeneracies in the modeling could be broken through observations of white dwarfs in these systems or through having more complete information about the chemical abundances of BSSs.

It would be interesting to investigate the Ba abundance of the APOGEE sample. This would help us distinguish which formation channel is more favorable. Another interesting element to look into is europium, which probes the rapid neutron capture processes. The r-process elements can tell us more about the environment the

stars come from. For example, the metal-poor stars in the ultra-faint dwarf galaxy Reticulum II show significant enhancement in r-process elements. This enhancement is not commonly seen in other ultra-faint dwarf galaxies, suggesting that a single event produced this enhancement, and it is thought to be a neutron star merger (Ji et al., 2016).

This work shows the importance of spectroscopic surveys for the study of BSSs as very large datasets are needed to identify these stars in the field of the Galactic halo. We are very limited by the size of our final sample, but future spectroscopic surveys like 4MOST or WEAVE will further help to expand the sample of BSSs. Our results show that the selection function plays a big role when looking for these exotic stars, e.g. a strict color cut on the blue end can significantly limit the number of stars in the final sample. Given our small sample of BSSs and complex selection functions of APOGEE and GALAH, we are unable to make any conclusions about the binary fraction of populations in the Galactic halo. Additionally, this work shows the importance of having the RVs from each individual visit of a star. It allows us to obtain a more complete information about the amplitude of the RV curve and to constrain the formation models better.

Conclusion

We use data from the spectroscopic surveys APOGEE and GALAH to find blue straggler stars in the Galactic halo of the Milky Way. After applying our selection criteria, using the Al and Na abundances to distinguish between the accreted and non-accreted stars, removing any cluster members, and inspecting the spectra, we end up with a small sample of blue straggler stars located in the field of the Galactic halo.

We take advantage of the measured chemical abundances and show the abundance patterns present in the final sample. We see that making the cut in [Al/Fe] and [Na/Fe] results in an accreted sample that is consistent with the α-low population present in the halo. Certain elemental abundances get significantly altered in the process of mass transfer, mainly the Li and Ba, and we use them to constrain the formation models of BSSs. The vast majority of stars show radial velocity variations ($\Delta v_r > 1$ km/s). This is consistent with our expectation that BSSs form mainly through binary star evolution and most of them should therefore be in a binary system. This also shows that a large fraction of the final sample are genuine BSSs. We determine the masses of these stars using isochrone fitting, which helps us constrain their formation channels. We find that there is a systematic offset between masses determined in the CMD and in the Kiel diagram. We conclude that mass estimates from the CMD are more reliable, since the effective temperature of stars is underestimated, leading to underestimated mass estimates when using the Kiel diagram.

We generate a large number of model BSSs using the Binary Star Evolution code, and compare this synthetic sample with the observed properties of BSSs. In the generated sample, we find a correlation between the mass of the BSS, the orbital period, and its formation channel. From the determination of formation channels, we conclude that the accreted and non-accreted samples are not inconsistent with being the same. The mass transfer of types B, B+C, C, and D are present throughout the metallicity range. Type B appears to be the dominant formation channel for the highest metallicity bin, likely due to the fact that this bin also contains the most massive stars, which can only be explained with mass transfer from a red giant.

After comparing the RV variations between the generated and observed sample, we find a systematic offset between the observations and predictions, where the models predict higher Δv_r than is observed in BSSs. We suggest that this is caused by the eccentricity of the binaries. The models predict circular orbits for post-mass-transfer systems, which is not consistent with observations. Orbital eccentricity in the generated BSSs would lower the synthetic Δv_r, potentially explaining the offset.

The stars in the final sample contain some peculiar systems, such as an eclipsing

binary, single and double-lined spectroscopic binaries, rapidly rotating stars, etc. These systems often have to be treated individually. We present the results of a more detailed modeling for two stars, which have the RV curve measured. We are able to recreate the system 2M16355860+4551590 very well through type B or B+C mass transfer. We find that the other system 08160733+194151 can only be created via type B mass transfer. However, we are not able to reproduce the higher eccentricity that is observed in both of these systems. This shows the need for new models that would be able to explain the higher eccentricity in some of these post-mass-transfer systems.

This work shows the importance of spectroscopic surveys for the study of BSSs in the field of the Galactic halo as observations of many stars are needed to find a small sample of these exotic stars. Selection effects of the surveys play a big role in how many stars end up in the final sample. Simpler selection functions of the surveys and larger sample of accreted BSSs would allow us to estimate the binary fraction in ancient dwarf galaxies. Future spectroscopic surveys will provide more insight into the formation and characteristics of these rare objects.

Bibliography

Abate, C., Pols, O. R., Izzard, R. G., Mohamed, S. S., & de Mink, S. E. 2013, Astronomy & Astrophysics, 552, A26, doi: 10.1051/0004-6361/201220007

Abdurro'uf, Accetta, K., Aerts, C., et al. 2022, The Astrophysical Journal Supplement Series, 259, 35, doi: 10.3847/1538-4365/ac4414

Arnett, D. 1996, Supernovae and Nucleosynthesis: An Investigation of the History of Matter from the Big Bang to the Present (Princeton University Press)

Asplund, M., Amarsi, A. M., & Grevesse, N. 2021, Astronomy & Astrophysics, 653, A141, doi: 10.1051/0004-6361/202140445

Bailer-Jones, C. A. L., Rybizki, J., Fouesneau, M., Demleitner, M., & Andrae, R. 2021, The Astronomical Journal, 161, 147, doi: 10.3847/1538-3881/abd806

Belokurov, V., Erkal, D., Evans, N. W., Koposov, S. E., & Deason, A. J. 2018, Monthly Notices of the Royal Astronomical Society, 478, 611, doi: 10.1093/mnras/sty982

Bensby, T., Feltzing, S., & Oey, M. S. 2014, Astronomy and Astrophysics, 562, A71, doi: 10.1051/0004-6361/201322631

Bensby, T., Feltzing, S., Gould, A., et al. 2017, Astronomy and Astrophysics, 605, A89, doi: 10.1051/0004-6361/201730560

Bidelman, W. P., & Keenan, P. C. 1951, Astrophysical Journal, 114, 473, doi: 10.1086/145488

Bonačić Marinović, A. A., Glebbeek, E., & Pols, O. R. 2008, Astronomy and Astrophysics, 480, 797, doi: 10.1051/0004-6361:20078297

Bonidie, V., Court, T., Daher, C. M., et al. 2022, The Astrophysical Journal Letters, 933, L18, doi: 10.3847/2041-8213/ac79af

Bovy, J. 2015, The Astrophysical Journal Supplement Series, 216, 29, doi: 10.1088/0067-0049/216/2/29

Bovy, J., & Rix, H.-W. 2013, The Astrophysical Journal, 779, 115, doi: 10.1088/0004-637X/779/2/115

Bressan, A., Marigo, P., Girardi, L., et al. 2012, Monthly Notices of the Royal Astronomical Society, 427, 127, doi: 10.1111/j.1365-2966.2012.21948.x

Buder, S., Asplund, M., Duong, L., et al. 2018, Monthly Notices of the Royal Astronomical Society, 478, 4513, doi: 10.1093/mnras/sty1281

Buder, S., Sharma, S., Kos, J., et al. 2021, Monthly Notices of the Royal Astronomical Society, 506, 150, doi: 10.1093/mnras/stab1242

Buder, S., Lind, K., Ness, M. K., et al. 2022, Monthly Notices of the Royal Astronomical Society, 510, 2407, doi: 10.1093/mnras/stab3504

Carney, B. W., Latham, D. W., Laird, J. B., Grant, C. E., & Morse, J. A. 2001, The Astronomical Journal, 122, 3419, doi: 10.1086/324233

Carollo, D., Beers, T. C., Lee, Y. S., et al. 2007, Nature, 450, 1020, doi: 10.1038/nature06460

Casagrande, L., & VandenBerg, D. A. 2018, Monthly Notices of the Royal Astronomical Society, 479, L102, doi: 10.1093/mnrasl/sly104

Charbonnel, C., & Talon, S. 2005, Science, 309, 2189, doi: 10.1126/science.1116849

Das, P., Hawkins, K., & Jofré, P. 2020, Monthly Notices of the Royal Astronomical Society, 493, 5195, doi: 10.1093/mnras/stz3537

Dermine, T., Izzard, R. G., Jorissen, A., & Van Winckel, H. 2013, Astronomy & Astrophysics, 551, A50, doi: 10.1051/0004-6361/201219430

Eggleton, P. P. 1983, Astrophysical Journal, 268, 368, doi: 10.1086/160960

Eldridge, J. J., & Tout, C. A. 2019, The Structure and Evolution of Stars (World Scientific), doi: 10.1142/p974

Escorza, A., Siess, L., Van Winckel, H., & Jorissen, A. 2020, Astronomy & Astrophysics, 639, A24, doi: 10.1051/0004-6361/202037487

Ferraro, F. R., Sabbi, E., Gratton, R., et al. 2006, The Astrophysical Journal, 647, L53, doi: 10.1086/507327

Feuillet, D. K., Feltzing, S., Sahlholdt, C. L., & Casagrande, L. 2020, Monthly Notices of the Royal Astronomical Society, 497, 109, doi: 10.1093/mnras/staa1888

Feuillet, D. K., Sahlholdt, C. L., Feltzing, S., & Casagrande, L. 2021, Monthly Notices of the Royal Astronomical Society, 508, 1489, doi: 10.1093/mnras/stab2614

Gaia Collaboration, Brown, A. G. A., Vallenari, A., et al. 2018a, Astronomy & Astrophysics, 616, A1, doi: 10.1051/0004-6361/201833051

Gaia Collaboration, Babusiaux, C., van Leeuwen, F., et al. 2018b, Astronomy & Astrophysics, 616, A10, doi: 10.1051/0004-6361/201832843

Gaia Collaboration, Vallenari, A., Brown, A. G. A., et al. 2022, arXiv e-prints, arXiv:2208.00211. https://arxiv.org/abs/2208.00211

Gallino, R., Arlandini, C., Busso, M., et al. 1998, The Astrophysical Journal, 497, 388, doi: 10.1086/305437

Gao, X., Lind, K., Amarsi, A. M., et al. 2020, Monthly Notices of the Royal Astronomical Society: Letters, 497, L30, doi: 10.1093/mnrasl/slaa109

Gillett, S. L. 1988, Astronomical Journal, 96, 1967, doi: 10.1086/114944

Glaspey, J. W., Pritchet, C. J., & Stetson, P. B. 1994, Astronomical Journal, 108, 271, doi: 10.1086/117067

GRAVITY Collaboration, Abuter, R., Amorim, A., et al. 2019, Astronomy & Astrophysics, 625, L10, doi: 10.1051/0004-6361/201935656

Hasselquist, S., Hayes, C. R., Lian, J., et al. 2021, The Astrophysical Journal, 923, 172, doi: 10.3847/1538-4357/ac25f9

Hawkins, K., Jofré, P., Masseron, T., & Gilmore, G. 2015, Monthly Notices of the Royal Astronomical Society, 453, 758, doi: 10.1093/mnras/stv1586

Hekker, S., & Johnson, J. A. 2019, Monthly Notices of the Royal Astronomical Society, 487, 4343, doi: 10.1093/mnras/stz1554

Helmi, A. 2020, Annual Review of Astronomy and Astrophysics, 58, 205, doi: 10.1146/annurev-astro-032620-021917

Helmi, A., Babusiaux, C., Koppelman, H. H., et al. 2018, Nature, 563, 85, doi: 10.1038/s41586-018-0625-x

Hurley, J. R., Pols, O. R., & Tout, C. A. 2000, Monthly Notices of the Royal Astronomical Society, 315, 543, doi: 10.1046/j.1365-8711.2000.03426.x

Hurley, J. R., Tout, C. A., & Pols, O. R. 2002, Monthly Notices of the Royal Astronomical Society, 329, 897, doi: 10.1046/j.1365-8711.2002.05038.x

Izzard, R. G., Dermine, T., & Church, R. P. 2010, Astronomy and Astrophysics, 523, A10, doi: 10.1051/0004-6361/201015254

Ji, A. P., Frebel, A., Chiti, A., & Simon, J. D. 2016, Nature, 531, 610, doi: 10.1038/nature17425

Jofré, P., & Weiss, A. 2011, Astronomy & Astrophysics, 533, A59, doi: 10.1051/0004-6361/201117131

Kharchenko, N. V., Piskunov, A. E., Schilbach, E., Röser, S., & Scholz, R. D. 2013, Astronomy & Astrophysics, 558, A53, doi: 10.1051/0004-6361/201322302

Knigge, C., Leigh, N., & Sills, A. 2009, Nature, 457, 288, doi: 10.1038/nature07635

Kobayashi, C., Leung, S.-C., & Nomoto, K. 2020, The Astrophysical Journal, 895, 138, doi: 10.3847/1538-4357/ab8e44

Kobayashi, C., Umeda, H., Nomoto, K., Tominaga, N., & Ohkubo, T. 2006, The Astrophysical Journal, 653, 1145, doi: 10.1086/508914

Kounkel, M., Covey, K. R., Stassun, K. G., et al. 2021, The Astronomical Journal, 162, 184, doi: 10.3847/1538-3881/ac1798

Kroupa, P. 2001, Monthly Notices of the Royal Astronomical Society, 322, 231, doi: 10.1046/j.1365-8711.2001.04022.x

Majewski, S. R., Schiavon, R. P., Frinchaboy, P. M., et al. 2017, The Astronomical Journal, 154, 94, doi: 10.3847/1538-3881/aa784d

Maxted, P. F. L., & Hutcheon, R. J. 2018, Astronomy & Astrophysics, 616, A38, doi: 10.1051/0004-6361/201732463

McWilliam, A., Wallerstein, G., & Mottini, M. 2013, The Astrophysical Journal, 778, 149, doi: 10.1088/0004-637X/778/2/149

Meyers, R. A. 1992, Encyclopedia of physical sciences and technology (Academic Press)

Milliman, K. E., Mathieu, R. D., & Schuler, S. C. 2015, The Astronomical Journal, 150, 84, doi: 10.1088/0004-6256/150/3/84

Moe, M., & Di Stefano, R. 2017, The Astrophysical Journal Supplement Series, 230, 15, doi: 10.3847/1538-4365/aa6fb6

Moe, M., Kratter, K. M., & Badenes, C. 2019, The Astrophysical Journal, 875, 61, doi: 10.3847/1538-4357/ab0d88

Nissen, P. E., & Schuster, W. J. 2010, Astronomy and Astrophysics, 511, L10, doi: 10.1051/0004-6361/200913877

North, P., Jorissen, A., & Mayor, M. 2000, in The Carbon Star Phenomenon, ed. R. F. Wing, Vol. 177, 269

Paczyński, B. 1971, Annual Review of Astronomy and Astrophysics, 9, 183, doi: 10.1146/annurev.aa.09.090171.001151

Padmanabhan, T. 2001, Theoretical Astrophysics - Volume 2, Stars and Stellar Systems, Vol. 2 (Cambridge University Press), doi: 10.2277/0521562414

Pavlovskii, K., & Ivanova, N. 2015, Monthly Notices of the Royal Astronomical Society, 449, 4415, doi: 10.1093/mnras/stv619

Perets, H. B., & Fabrycky, D. C. 2009, The Astrophysical Journal, 697, 1048, doi: 10.1088/0004-637X/697/2/1048

Pinsonneault, M. 1997, Annual Review of Astronomy and Astrophysics, 35, 557, doi: 10.1146/annurev.astro.35.1.557

Pourbaix, D., Tokovinin, A. A., Batten, A. H., et al. 2004, Astronomy and Astrophysics, 424, 727, doi: 10.1051/0004-6361:20041213

Preece, H. P., Hamers, A. S., Neunteufel, P. G., Schaefer, A. L., & Tout, C. A. 2022, The Astrophysical Journal, 933, 25, doi: 10.3847/1538-4357/ac6fe3

Queiroz, A. B. A., Anders, F., Chiappini, C., et al. 2020, Astronomy & Astrophysics, 638, A76, doi: 10.1051/0004-6361/201937364

Raghavan, D., McAlister, H. A., Henry, T. J., et al. 2010, The Astrophysical Journal Supplement, 190, 1, doi: 10.1088/0067-0049/190/1/1

Reggiani, H., Meléndez, J., Kobayashi, C., Karakas, A., & Placco, V. 2017, Astronomy & Astrophysics, 608, A46, doi: 10.1051/0004-6361/201730750

Roederer, I. U., Preston, G. W., Thompson, I. B., et al. 2014, The Astronomical Journal, 147, 136, doi: 10.1088/0004-6256/147/6/136

Ryan, S. G., Beers, T. C., Kajino, T., & Rosolankova, K. 2001, The Astrophysical Journal, 547, 231, doi: 10.1086/318338

Sahlholdt, C. L., & Lindegren, L. 2021, Monthly Notices of the Royal Astronomical Society, 502, 845, doi: 10.1093/mnras/stab034

Sandage, A. R. 1953, Astronomical Journal, 58, 61, doi: 10.1086/106822

Santana, F. A., Muñoz, R. R., Geha, M., et al. 2013, The Astrophysical Journal, 774, 106, doi: 10.1088/0004-637X/774/2/106

Sills, A. 2016, Memorie della Societa Astronomica Italiana, 87, 475

Spite, F., & Spite, M. 1982, Astronomy and Astrophysics, 115, 357

Traven, G., Feltzing, S., Merle, T., et al. 2020, Astronomy & Astrophysics, 638, A145, doi: 10.1051/0004-6361/202037484

Umeda, H., & Nomoto, K. 2002, The Astrophysical Journal, 565, 385, doi: 10.1086/323946

Vagnozzi, S. 2019, Atoms, 7, 41, doi: 10.3390/atoms7020041

Vos, J., Bobrick, A., & Vučković, M. 2020, Astronomy & Astrophysics, 641, A163, doi: 10.1051/0004-6361/201937195

Wenger, M., Ochsenbein, F., Egret, D., et al. 2000, Astronomy and Astrophysics Supplement, 143, 9, doi: 10.1051/aas:2000332

Winter, A. J., & Clarke, C. J. 2023, Monthly Notices of the Royal Astronomical Society, 521, 1646, doi: 10.1093/mnras/stad312

Wyse, R. F. G., Moe, M., & Kratter, K. M. 2020, Monthly Notices of the Royal Astronomical Society, 493, 6109, doi: 10.1093/mnras/staa731

Ziegler, C., Law, N. M., Baranec, C., Riddle, R. L., & Fuchs, J. T. 2015, The Astrophysical Journal, 804, 30, doi: 10.1088/0004-637X/804/1/30

Appendix A

The appendix contains tables summarizing what we know about the final sample of stars and showing the results of BSE modeling. In Tables A.1 and A.2, we show the dereddened color index $(\mathrm{BP}-\mathrm{RP})_0$, absolute G-band magnitude, effective temperature T_{eff}, surface gravity $\log g$, metallicity [Fe/H], distance d, its uncertainty σ_d, aluminum abundance [Al/Fe] or sodium abundance [Na/Fe], and finally a note describing the classification or interesting findings about the stars in the final sample. Each star also has a number index, which is used in figures throughout this work.

Tables A.3 and A.4 show the radial velocities, the RV variation Δv_r determined from those values, predicted Δv_r from using the generated BSE sample of BSSs, lithium abundance A(Li) (only for the GALAH sample), barium abundance [Ba/Fe] (only for the GALAH sample), isochrone mass M_* determined using maximum likelihood estimation in the CMD. We then show possible formation channels from the analysis of the generated BSSs. We made a box around each observed star in the CMD, containing ≈100 generated BSSs. We list what percentage of cases formed through each type of mass transfer. Type A referring to the case when the donor is a MS star, HG when the donor is in the Hertzsprung gap, type B when it is a RGB star, type C when it is an AGB star, type B+C when both type B and C mass transfers happen during the evolution of a star, and type D referring to wind accretion scenario. The percentages do not always add up to 100% as there are cases when e.g. both HG and type B mass transfer occur and since we are not distinguishing between these special cases, we end up double counting. However, there are only a few of these rare cases.

Table A.1: Magnitudes, stellar parameters, and other important parameters for the APOGEE sample. The accreted and non-accreted samples are separated by the horizontal line.

Index	APOGEE_ID	$(BP-RP)_0$ [mag]	M_G [mag]	$T_{\rm eff}$ [K]	$\log g$	[Fe/H]	d [pc]	σ_d [pc]	[Al/Fe]	Note
1	2M16254476+2850475	0.562	3.57	5793	3.87	-1.52	290.4	1.4	-0.20	
2	2M16355860+4551590	0.579	4.21	6395	4.29	-1.13	252.2	3.5	-0.34	SBI[1]
3	2M14531026+4814485	0.588	3.65	5759	4.01	-1.81	249.3	0.9	-0.21	
4	2M13031533+5550458	0.599	3.69	5813	3.94	-1.52	584.9	4.0	-0.38	
5	2M16024225-2029174	0.739	3.12	5895	4.23	-1.15	741.8	8.2	-0.23	Eclipsing binary[2]
6	2M12052096+1940445	0.526	3.01	6249	3.98	-1.33	478.7	19.7	-0.43	Resolved companion[3]
7	2M16062260+0522427	0.442	3.59	6867	4.01	-1.58	351.6	2.9	-0.27	
1	2M19223545+7448389	0.656	2.50	5747	3.74	-0.58	757.1	28.6	0.00	
2	2M01055860-7617508	0.528	2.83	6473	3.85	-0.66	2395.1	113.3	0.66	
3	2M14243398+5035364	0.635	3.33	5629	3.67	-2.00	1007.9	12.5	0.45	
4	2M13534834+0211191	0.638	3.54	5940	3.92	-0.92	814.7	11.5	0.02	
5	2M08442470+2447483	0.380	3.39	6559	4.16	-1.42	135.5	0.3	-0.12	Li depleted[4]
6	2M15254880+2720149	0.529	2.84	6018	3.72	-0.71	403.0	3.2	0.16	
7	2M00195002-1323484	0.584	2.85	6352	3.92	-0.86	492.1	9.3	0.18	
8	2M22004004-1145315	0.584	1.68	5773	3.47	-1.62	1291.8	35.9	-0.06	
9	2M23420726-1057219	0.711	2.86	6028	3.61	-0.85	2476.7	205.3	0.26	
10	2M19260321+4421315	0.591	3.91	5790	4.34	-1.34	162.9	1.6	-0.10	
11	2M22422590+2345117	0.678	3.11	6097	3.78	-0.95	1123.7	22.0	0.15	
12	2M14590831+3022494	0.713	3.27	5215	3.04	-1.67	414.1	5.8	0.60	
13	2M10253869+0118570	0.766	2.74	5790	3.74	-0.56	775.3	18.6	0.36	
14	2M08301131+2037509	0.627	3.60	5993	4.24	-0.53	351.0	3.2	0.29	
15	2M17455483+6544596	0.647	3.48	5182	3.57	-1.88	309.2	1.0	-0.07	
16	2M18180506+6214062	0.580	3.52	6312	4.21	-0.53	265.4	0.7	0.30	
17	2M05513901-5951092	0.603	2.81	4825	3.45	-1.03	618.2	5.6	-0.13	Also in GALAH
18	2M12052336+5305294	0.632	3.50	5590	3.85	-1.43	443.1	2.5	-0.11	
19	2M07250746-6745394	0.433	2.52	5421	3.19	-0.71	579.3	3.9	0.06	
20	2M15492948+2847132	0.363	3.13	6837	4.02	-1.09	398.5	4.5	0.02	

[1]Pourbaix et al. (2004), [2]Maxted & Hutcheon (2018), [3]Ziegler et al. (2015), [4]Glaspey et al. (1994).

Table A.2: Magnitudes, stellar parameters, and other important parameters for the GALAH sample. The accreted and non-accreted samples are separated by the horizontal line.

Index	star_id	$(BP-RP)_0$ [mag]	M_G [mag]	$T_{\rm eff}$ [K]	$\log g$	[Fe/H]	d [pc]	σ_d [pc]	[Na/Fe]	Note
1	10032057-3154168	0.592	3.90	6046	4.18	-1.11	452.7	2.5	-0.19	GSE star[1]
2	10372825+0115579	0.734	3.03	5743	3.74	-1.13	1130.8	22.5	-0.23	
3	14024428-0929107	0.623	2.60	5915	3.84	-0.85	1083.1	36.1	-0.06	
4	22424052-5013383	0.519	2.02	6369	3.71	-0.80	1162.3	36.8	-0.08	
5	05000611-6745566	0.521	3.44	6094	4.01	-1.16	632.8	5.1	-0.09	
6	08441597-0907024	0.629	3.39	5918	3.93	-1.22	575.5	4.8	-0.14	GSE star[1]
7	14125353-4417194	0.484	3.02	6502	3.91	-0.87	929.3	26.9	-0.19	
1	12135303-0958506	0.435	2.63	6546	4.07	-0.96	631.4	20.5	0.30	
2	01072738-6514100	0.472	2.77	6432	4.02	-0.78	672.6	5.2	0.18	
3	15450652-1953387	0.585	3.55	6222	3.88	-2.41	1375.9	48.7	0.80	
4	12390733-3906151	0.655	3.43	5725	3.92	-0.84	714.5	10.5	0.08	
5	11523688+0329462	0.688	3.37	5829	3.86	-1.16	931.1	12.8	0.26	
6	22115018-1434293	0.438	2.72	6648	4.06	-0.70	769.7	8.3	0.33	
7	04434542-5844113	0.532	2.74	6293	4.03	-0.58	1241.6	32.7	0.25	
8	10153448-2201378	0.616	3.56	5782	3.97	-1.00	834.2	16.0	0.09	
9	18283281-5857107	0.683	3.04	5831	3.71	-1.68	948.3	11.7	0.25	
10	00042406-2121199	0.675	3.22	5750	3.61	-2.10	1870.4	113.0	0.71	
11	16100596-3054088	0.596	2.96	5841	3.77	-1.39	650.8	5.5	0.31	SBII[2]
12	05145893-4611484	0.570	3.48	6097	3.96	-1.94	661.6	5.3	0.42	
13	15333857-2002575	0.593	3.02	6247	3.94	-0.65	1705.3	59.3	0.21	
14	17521305-4816106	0.582	2.96	6449	4.00	-0.61	340.0	11.2	0.30	
15	14050663-3341137	0.452	2.01	6556	3.78	-0.86	1154.6	25.9	0.19	
16	04374970-0123263	0.712	3.29	5751	3.98	-0.65	718.4	13.9	0.26	
17	09485429-1805263	0.616	1.50	5955	3.41	-0.74	1724.5	48.6	0.07	
18	10592407-2838219	0.542	3.22	6437	4.08	-0.71	1089.6	17.2	0.18	
19	15153021-2808452	0.636	3.56	5947	3.95	-1.27	574.3	5.3	-0.01	
20	11512742-2815296	0.466	2.92	6548	3.93	-0.87	909.0	18.1	0.28	
21	05585235-3049356	0.512	3.14	6482	4.07	-0.62	731.2	6.6	0.39	
22	16084525-7014246	0.599	3.99	6060	4.14	-2.05	787.4	9.4	0.35	
23	00531962-2639202	0.618	3.27	5995	3.80	-2.17	2208.5	144.9	1.32	
24	11390587-2645238	0.739	3.06	5418	3.73	-0.67	1002.4	21.3	0.14	
25	13152913-1321116	0.599	3.18	6216	3.97	-1.07	1085.8	18.4	0.06	
26	12445211-3525466	0.693	3.23	5785	3.85	-1.46	834.0	10.3	0.15	
27	13243975-3428228	0.502	1.89	6312	3.66	-0.60	1878.9	70.4	0.23	
28	04480709-2832231	0.453	2.47	6544	3.91	-0.79	1229.5	38.1	0.23	
29	13092954-3826152	0.531	2.91	6382	4.03	-0.69	821.8	23.7	0.09	
30	20342174-2844446	0.368	2.90	6948	4.13	-0.93	777.8	9.8	0.15	
31	22174515-7255044	0.748	3.08	5930	3.84	-0.67	947.5	14.2	0.12	
32	20390862-3439106	0.626	3.60	5986	3.95	-1.29	722.5	7.8	0.20	
33	21301880-0334222	0.535	3.24	6491	4.08	-0.69	875.2	17.0	0.27	
34	13380083-0813382	0.582	3.97	6290	4.21	-2.11	411.6	3.7	0.56	
35	05501208-6017209	0.550	3.88	6512	4.21	-1.09	528.8	7.3	0.54	
36	18313894-5427314	0.757	1.83	5121	2.87	-1.55	1426.3	30.0	0.28	Giant, not BSS
37	21573999+0200275	0.581	3.36	6181	4.48	-0.60	982.8	131.4	0.18	
38	13464918-3406505	0.357	3.20	6996	4.32	-0.77	1154.8	25.5	0.18	
39	14231032-2248065	0.473	2.52	6432	3.88	-0.84	909.1	15.7	0.17	
40	05525787-5510343	0.567	4.15	6228	4.24	-2.15	332.1	1.2	0.78	
41	22485965-7625403	0.518	2.57	6590	3.94	-0.90	712.2	60.0	0.22	
42	08160733+1941519	0.574	4.11	6329	4.27	-2.31	239.6	1.9	0.88	SBI[3]
43	15051254-2622071	0.725	3.10	5765	3.76	-0.77	1007.9	29.9	0.09	
44	12283812-0106341	0.400	2.80	6832	4.05	-0.76	1362.0	56.7	0.32	
45	03163723-5755051	0.609	3.50	5850	3.99	-1.14	838.5	8.5	0.05	

[1]Helmi et al. (2018), [2]Traven et al. (2020), [3]Pourbaix et al. (2004).

Table A.3: Radial velocities, quantities that help us constrain the models, and results of the modeling for the APOGEE sample. The accreted and non-accreted samples are separated by the horizontal line.

Index	APOGEE_ID	$N_{\rm obs}$	RV APOGEE [km/s]	RV GaiaDR2 [km/s]	RV GaiaDR3 [km/s]	Δv_r [km/s]	BSE Δv_r [km/s]	M_* [$M_\odot$]	Type A	HG	Type B	Type B+C	Type C	Type D
1	2M16254476+2850475	6	15.9 ± 0.1	15.5 ± 0.8	14.9 ± 0.7	1.1	12.2 ± 6.6	0.8 ± 0.1	0%	2%	36%	61%	1%	0%
2	2M16355860+4551590	5	-239.7 ± 1.4		-248.0 ± 3.3	10.2	15.1 ± 8.4	0.9 ± 0.1	2%	3%	95%	0%	0%	0%
3	2M14531026+4814485	9	-156.8 ± 0.2	-157.3 ± 0.5	-156.7 ± 0.4	1.1	12.9 ± 6.5	0.8 ± 0.1	0%	2%	9%	76%	13%	0%
4	2M13031533+5550458	10	37.1 ± 0.4		36.4 ± 1.4	1.5	10.7 ± 5.9	0.8 ± 0.1	0%	1%	6%	66%	27%	0%
5	2M16024225-2029174	8	273.7 ± 0.0	261.2 ± 5.8	258.3 ± 2.7	58.6	1.3 ± 2.2	0.9 ± 0.0	0%	0%	0%	4%	14%	82%
6	2M12052096+1940445	13	29.6 ± 0.3	29.2 ± 0.8	28.6 ± 1.8	1.6	16.4 ± 5.6	0.9 ± 0.0	0%	2%	71%	27%	0%	0%
7	2M16062260+0522427	22	-217.8 ± 0.4	-218.2 ± 1.4	-216.5 ± 0.8	2.0	21.7 ± 5.8	0.9 ± 0.1	0%	1%	99%	0%	0%	0%
1	2M19223545+7448389	5	-212.9 ± 0.1	-216.0 ± 2.1	-217.1 ± 1.4	4.2	11.0 ± 6.0	1.2 ± 0.0	0%	3%	42%	47%	9%	0%
2	2M01055860-7617508	19	114.4 ± 6.2			22.6	16.4 ± 5.2	1.1 ± 0.1	0%	1%	78%	21%	0%	0%
3	2M14243398+5035364	10	-139.4 ± 1.2		-136.6 ± 2.6	3.7	4.3 ± 3.9	0.8 ± 0.0	0%	0%	0%	10%	41%	49%
4	2M13534834+0211191	8	27.7 ± 0.3		32.4 ± 3.9	5.0	2.5 ± 4.1	0.9 ± 0.1	0%	1%	0%	0%	15%	84%
5	2M08442470+2447483	5	59.1 ± 0.5	57.9 ± 0.2	57.2 ± 0.2	2.2	16.9 ± 6.9	1.0 ± 0.1	0%	3%	97%	0%	0%	0%
6	2M15254880+2720149	5	-123.2 ± 0.1	-122.8 ± 1.0	-123.5 ± 0.4	0.7	13.6 ± 5.8	1.1 ± 0.1	0%	1%	77%	22%	0%	0%
7	2M00195002-1323484	8	-83.6 ± 0.2	-84.5 ± 1.3	-83.9 ± 0.5	1.2	14.0 ± 5.5	1.0 ± 0.1	0%	2%	39%	55%	4%	0%
8	2M22004004-1145315	4	-101.4 ± 0.0	-107.7 ± 5.1	-103.3 ± 3.6	6.3	13.2 ± 5.4	1.2 ± 0.0	0%	0%	100%	0%	0%	0%
9	2M23420726-1057219	16	-36.5 ± 4.8			12.8	8.4 ± 6.4	1.0 ± 0.0	0%	1%	6%	36%	35%	22%
10	2M19260321+4421315	6	-296.5 ± 1.8	-295.3 ± 1.4	-292.2 ± 2.4	6.2	12.8 ± 6.9	0.8 ± 0.1	1%	5%	29%	60%	5%	0%
11	2M22422590+2345117	5	-223.1 ± 0.4		-223.5 ± 3.5	0.7	3.8 ± 4.2	0.9 ± 0.0	0%	1%	2%	15%	36%	46%
12	2M14590831+3022494	5	-45.0 ± 0.1	-43.6 ± 0.6	-45.3 ± 0.4	1.7	0.5 ± 1.0	0.8 ± 0.0	0%	0%	0%	0%	8%	92%
13	2M10253869+0118570	6	78.7 ± 0.1	76.5 ± 1.8	80.0 ± 1.7	3.5	7.2 ± 6.8	1.1 ± 0.0	0%	1%	7%	33%	28%	31%
14	2M08301131+2037509	4	134.8 ± 0.0	134.9 ± 1.9	134.2 ± 0.8	0.7	2.9 ± 3.2	1.0 ± 0.1	0%	0%	0%	7%	31%	63%
15	2M17455483+6544596	4	-178.1 ± 0.0	-180.1 ± 1.2	-179.2 ± 0.5	2.0	1.5 ± 2.9	0.8 ± 0.0	0%	1%	0%	0%	13%	86%
16	2M18180506+6214062	5	-102.5 ± 0.3	-102.4 ± 1.1	-103.5 ± 0.5	1.1	10.6 ± 5.5	1.0 ± 0.1	0%	2%	14%	70%	14%	0%
17	2M05513901-5951092	4	166.1 ± 0.0	4.4 ± 14.7	16.1 ± 9.0	161.7	10.6 ± 6.2	1.0 ± 0.0	0%	2%	29%	58%	11%	0%
18	2M12052336+5305294	11	-157.4 ± 0.1	-158.6 ± 1.9	-158.4 ± 0.8	1.3	3.1 ± 4.3	0.8 ± 0.1	0%	1%	0%	0%	23%	76%
19	2M07250746-6745394	4	134.5 ± 0.0	16.5 ± 3.4	2.9 ± 4.9	131.6	12.9 ± 6.3	1.2 ± 0.1	1%	3%	97%	0%	0%	0%
20	2M15492948+2847132	10	-189.1 ± 0.7	-190.0 ± 1.4	-185.7 ± 22.3	4.4	18.0 ± 6.3	1.1 ± 0.1	0%	0%	100%	0%	0%	0%

Table A.4: Radial velocities, quantities that help us constrain the models, and results of the modeling for the GALAH sample. The accreted and non-accreted samples are separated by the horizontal line.

Index	star_id	RV GALAH [km/s]	RV GaiaDR2 [km/s]	RV GaiaDR3 [km/s]	Δv_r [km/s]	BSE Δv_r [km/s]	A(Li)	[Ba/Fe]	M_* [$M_\odot$]	Type A	HG	Type B	Type B+C	Type C	Type D
1	10032057-3154168	296.7 ± 0.2	298.3 ± 1.1	297.5 ± 0.8	1.6	9.7 ± 6.9	2.18	-0.05	0.86 ± 0.11	0%	4%	29%	62%	5%	0%
2	10372825+0115579	179.4 ± 0.3		193.6 ± 7.9	14.2	1.8 ± 2.8	2.31	-0.18	0.88 ± 0.04	0%	0%	0%	17%	24%	59%
3	14024428-0929107	50.0 ± 0.1		60.5 ± 2.5	10.5	5.6 ± 5.1		0.24	1.05 ± 0.03	0%	3%	37%	53%	7%	0%
4	22424052-5013383	-0.1 ± 0.2	10.8 ± 3.1	5.2 ± 1.6	10.9	10.7 ± 5.9		0.05	1.27 ± 0.06	0%	0%	100%	0%	0%	0%
5	05000611-6745566	157.0 ± 0.1	157.7 ± 3.3	154.7 ± 2.1	3.0	11.3 ± 7.6	1.68	-0.06	0.91 ± 0.11	0%	3%	91%	6%	0%	0%
6	08441597-0907024	58.3 ± 0.2	58.7 ± 2.1	58.8 ± 1.3	0.5	2.8 ± 3.1	2.38	0.02	0.84 ± 0.06	0%	1%	0%	10%	38%	52%
7	14125353-4417194	330.5 ± 0.2		332.1 ± 3.8	1.6	6.5 ± 5.5	2.32	-0.01	1.05 ± 0.06	0%	4%	96%	0%	0%	0%
1	12135303-0958506	57.3 ± 0.2	52.7 ± 3.9	51.5 ± 2.3	5.8	11.2 ± 6.7		-0.20	1.07 ± 0.07	1%	3%	97%	0%	0%	0%
2	01072738-6514100	25.6 ± 0.1		27.1 ± 1.0	1.6	7.3 ± 10.8		-0.16	1.11 ± 0.07	1%	3%	96%	0%	0%	0%
3	15450652-1953387	35.0 ± 1.6						0.88	0.77 ± 0.01	0%	2%	9%	73%	16%	0%
4	12390733-3906151	128.4 ± 0.2		128.8 ± 2.2	0.3	0.6 ± 1.0	1.91	-0.03	0.88 ± 0.12	0%	0%	0%	0%	11%	89%
5	11523688+0329462	62.9 ± 0.2		63.9 ± 2.6	1.1	0.2 ± 0.3	2.20	-0.03	0.82 ± 0.05	0%	0%	0%	0%	2%	98%
6	22115018-1434293	45.6 ± 0.3	48.6 ± 2.5	49.0 ± 1.2	3.5	11.8 ± 15.7		-0.25	1.18 ± 0.07	2%	3%	96%	0%	0%	0%
7	04434542-5844113	85.3 ± 0.1		83.9 ± 3.7	1.4	7.3 ± 5.5		-0.20	1.13 ± 0.08	0%	2%	79%	19%	0%	0%
8	10153448-2201378	279.4 ± 0.2		284.9 ± 5.3	5.5	2.2 ± 2.7	2.31	0.11	0.85 ± 0.12	0%	1%	1%	23%	40%	35%
9	18283281-5857107	200.5 ± 0.3		192.2 ± 3.0	8.3	2.0 ± 2.9	2.29	0.00	0.81 ± 0.04	0%	1%	2%	21%	39%	38%
10	00042406-2121199	17.2 ± 0.2					2.23	-0.12	0.75 ± 0.04	0%	0%	0%	3%	25%	73%
11	16100596-3054088	94.3 ± 0.2	119.4 ± 12.8		25.1	5.4 ± 4.8	1.97	-0.32	0.90 ± 0.04	0%	2%	19%	68%	12%	0%
12	05145893-4611484	157.7 ± 0.4		157.6 ± 2.1	0.0	5.4 ± 5.6	2.33	-0.02	0.77 ± 0.05	0%	1%	27%	64%	8%	0%
13	15333857-2002575	40.0 ± 0.1		38.9 ± 11.2	1.0	4.9 ± 5.5		-0.09	1.06 ± 0.11	0%	1%	16%	70%	13%	0%
14	17521305-4816106	76.2 ± 0.2	69.6 ± 2.5	71.1 ± 1.6	6.7	8.8 ± 5.7		-0.22	1.04 ± 0.10	0%	1%	28%	64%	7%	0%
15	14050663-3341137	217.3 ± 0.4	225.2 ± 8.7	219.9 ± 4.1	7.9	11.8 ± 6.4		-0.20	1.25 ± 0.03	0%	1%	99%	0%	0%	0%
16	04374970-0123263	0.1 ± 0.2		3.5 ± 1.6	3.4	0.3 ± 0.8		1.54	0.91 ± 0.04	0%	0%	0%	0%	7%	93%
17	09485429-1805263	155.4 ± 0.1		153.9 ± 2.3	1.5	6.4 ± 5.4		0.12	1.41 ± 0.03	0%	1%	99%	0%	0%	0%
18	10592407-2838219	169.0 ± 0.2		169.2 ± 3.0	0.1	6.8 ± 5.7	2.08	-0.14	1.18 ± 0.08	0%	0%	54%	46%	0%	0%
19	15153021-2808452	97.8 ± 0.2	93.0 ± 3.0	97.9 ± 3.9	4.9	1.3 ± 1.4	2.26	-0.07	0.81 ± 0.06	0%	0%	0%	0%	16%	84%
20	11512742-2815296	172.2 ± 0.3		170.2 ± 2.4	2.0	7.4 ± 8.0	2.29	-0.10	1.05 ± 0.06	1%	3%	96%	0%	0%	0%
21	05585235-3049356	97.0 ± 1.2	95.4 ± 3.9	94.5 ± 2.7	2.5	10.9 ± 6.1		-0.38	1.20 ± 0.07	0%	3%	86%	11%	0%	0%
22	16084525-7014246	163.6 ± 0.4		161.0 ± 3.7	2.6	5.6 ± 5.4	2.32	0.14	0.72 ± 0.13	1%	4%	27%	61%	7%	0%
23	00531962-2639202	35.1 ± 1.7					2.41	-0.05	0.77 ± 0.01	0%	1%	1%	37%	38%	23%
24	11390587-2645238	47.0 ± 0.1		42.6 ± 2.8	4.4	1.0 ± 2.0	1.34	-0.40	0.98 ± 0.02	0%	0%	0%	10%	20%	70%
25	13152913-1321116	56.6 ± 0.1		58.6 ± 5.6	2.0	5.2 ± 4.9		0.21	0.90 ± 0.05	0%	1%	6%	70%	22%	1%
26	12445211-3525466	146.2 ± 0.2		150.3 ± 2.3	4.1	0.5 ± 1.8	2.34	-0.19	0.79 ± 0.04	0%	0%	0%	0%	11%	89%
27	13243975-3428228	79.8 ± 0.2		72.8 ± 4.8	7.0	6.4 ± 5.7	2.01	-0.25	1.42 ± 0.05	0%	0%	100%	0%	0%	0%
28	04480709-2832231	31.9 ± 0.3		31.7 ± 3.3	0.2	6.8 ± 5.6		-0.20	1.16 ± 0.06	1%	3%	97%	0%	0%	0%
29	13092954-3826152	181.3 ± 0.2		184.0 ± 2.4	2.7	8.0 ± 5.7		-0.14	1.08 ± 0.06	0%	1%	70%	29%	0%	0%
30	20342174-2844446	105.5 ± 0.4		101.9 ± 3.0	3.6	8.6 ± 6.9		-0.31	1.10 ± 0.04	1%	5%	95%	0%	0%	0%
31	22174515-7255044	103.7 ± 0.1		102.3 ± 1.9	1.4	1.2 ± 2.2	1.91	-0.20	0.95 ± 0.02	0%	0%	0%	10%	16%	74%
32	20390862-3439106	12.5 ± 0.2		12.7 ± 2.0	0.3	1.9 ± 2.3	2.34	-0.11	0.79 ± 0.04	0%	0%	0%	8%	32%	60%
33	21301880-0334222	-130.4 ± 0.3		-136.8 ± 3.9	6.3	7.6 ± 5.8	2.28	-0.23	1.16 ± 0.09	0%	0%	65%	35%	0%	0%
34	13380083-0813382	18.0 ± 1.0	18.2 ± 2.8	18.1 ± 1.6	0.2	11.0 ± 7.1	2.34	0.02	0.72 ± 0.13	0%	7%	52%	40%	1%	0%
35	05501208-6017209	216.0 ± 2.7	232.3 ± 7.4	223.9 ± 3.8	16.3	11.5 ± 6.6	2.56	0.05	0.88 ± 0.08	0%	5%	92%	3%	0%	0%
36	18313894-5427314	233.9 ± 0.1		234.9 ± 2.0	0.9	7.8 ± 5.9		0.00	1.14 ± 0.04	0%	2%	74%	24%	0%	0%
37	21573999+0200275	-88.4 ± 0.1		-91.3 ± 6.8	3.0	5.0 ± 5.8	1.95	-0.24	1.02 ± 0.10	0%	2%	13%	70%	15%	0%
38	13464918-3406505	115.2 ± 0.6					2.53	-0.06	1.18 ± 0.05	0%	1%	99%	0%	0%	0%
39	14231032-2248065	152.8 ± 0.3		153.7 ± 2.4	0.9	6.9 ± 6.8		-0.07	1.13 ± 0.07	1%	3%	97%	0%	0%	0%
40	05525787-5510343	215.9 ± 1.0	216.5 ± 1.0		0.6	8.7 ± 10.0	2.27		0.77 ± 0.07	1%	6%	93%	0%	0%	0%
41	22485965-7625403	39.7 ± 0.3	43.6 ± 2.7	42.6 ± 4.2	3.9	11.3 ± 6.7	2.34	-0.26	1.08 ± 0.04	0%	2%	94%	4%	0%	0%
42	08160733+1941519	-58.5 ± 2.4	-58.8 ± 2.7	-61.8 ± 1.6	3.3	13.3 ± 12.4	2.21	0.27	0.75 ± 0.09	1%	7%	88%	4%	0%	0%
43	15051254-2622071	45.4 ± 0.1		47.4 ± 4.0	1.9	1.4 ± 2.8	1.90	-0.06	0.94 ± 0.03	0%	0%	0%	7%	20%	73%
44	12283812-0106341	81.1 ± 0.4		98.5 ± 10.2	17.4	8.6 ± 14.9	2.56	0.26	1.16 ± 0.05	2%	3%	96%	0%	0%	0%
45	03163723-5755051	155.4 ± 0.2		155.7 ± 3.3	0.4	3.0 ± 3.5	2.60	0.24	0.85 ± 0.13	0%	2%	1%	38%	40%	19%